Title

Spectroscopic Studies of Electronic States in Unconventional Superconductors

Author

Walker, Morgan

Publication Date

2024

Peer reviewed|Thesis/dissertation

Spectroscopic Studies of Electronic States in Unconventional Superconductors

By

MORGAN WALKER
DISSERTATION

Submitted in partial satisfaction of the requirements for the degree of

DOCTOR OF PHILOSOPHY

in

Physics

in the

OFFICE OF GRADUATE STUDIES

of the

UNIVERSITY OF CALIFORNIA

DAVIS

Approved:

Eduardo H. da Silva Neto, Chair

Valentin Taufour

Nicholas Curro

Committee in Charge

2024

Contents

List of Figures

List of Tables

Abstract

This work will present experimental results on two projects measuring the electronic properties of unconventional superconductors. The first project focuses on the iron-based superconductor system of $FeSe_{1-x}S_x$. We used scanning tunneling microscopy/spectroscopy (STM/S) to make detailed measurements of the electronic states of tetragonal $FeSe_{0.81}S_{0.19}$. We also performed theoretical band structure calculations that were calibrated by angle-resolved photoemission spectroscopy measurements for comparison. We utilize the high spatial resolution of the STM/S measurements to separately analyze modulations in the local density of states (LDOS) in regions near and away from iron-vacancies. This analysis revealed two types of features: (i) energy dispersive quasiparticle interference patterns which can explained by our band structure calculations and (ii) a much stronger modulation just above the Fermi level centered at $\mathbf{q} = 0.12$ Å^{-1} which does not disperse with energy and cannot be explained by our band structure model. Local rotational symmetry analysis shows that while the modulations are four-fold symmetric on average, they are actually comprised of small domains with two-fold symmetry. Statistical analysis demonstrates that the boundaries of these domains are spatially correlated with the locations of iron-vacancies.

The second project studies charge order in the La-based cuprate $La_{1.475}Nd_{0.4}Sr_{0.125}CuO_4$. We performed temperature and uniaxial strain dependent resonant x-ray scattering studies on the charge order and the low-temperature orthorhombic to low-temperature tetragonal (LTO-LTT) structural transition. Before applying any strain, we found a precursor charge order peak existing up to 200 K, well above the static charge order onset temperature. Upon applying uniaxial tensile strain of about 0.1%, we observed a reduction in the onset of charge order by 50 K and a 20 K reduction in the LTO-LTT transition temperature. We also saw a preference for the charge order to form in the direction of applied strain due to a 6 K difference in onset temperatures for the two directions.

Acknowledgements

First I would like to thank my parents and my sister, for supporting me always. They always selflessly sacrificed so that I could have opportunities they did not. They made sure I saw the world outside of my hometown, even knowing that exposure might one day lead me to move far away.

Next, I would like thank my advisor, Prof. Eduardo da Silva Neto, for the years of excellent research opportunity and mentorship. Especially I would like to thank him for going above and beyond to remain a present and attentive advisor from across the country. Other important research mentors and collaborators have helped me tremendously: Dr. Timothy Boyle, Dr. Alejandro Ruiz, and Professor Fabio Boschini, who taught me how to use the STM and guided me through my first beamtimes, and Dr. Adrian Gozar who helped me with paper writing in my final years. From the early days, Dr. Allen Majewski, who gave me my first experience in physics research, has continued to be an important cheerleader during graduate school. He also helped shape who I am as a mentor, which I find an important aspect of my development as a scientist. To that end, I owe many thanks to the junior students I have mentored and trained, particularly: Eli Baum, Journey Byland, Kirsty Scott, and Sophie Miller. Journey really deserves extra thanks since she grew all of my samples as well. You guys keep kicking ass out there. My committee members, Profs. Nick Curro and Valentin Taufour, have been especially helpful for conversations about our shared research interests. Prof. Shirley Chiang has served as a fabulous bonus mentor in my final years.

Friendship has been essential to thriving during graduate school, so I would like to thank all of my friends here in Davis, especially those from our first year cohort. We have all been through a lot together and have always leaned on each other throughout. Finally, I want to thank my best friend and partner, Daniel Polin, for unwavering understanding and support.

Chapter 1

Introduction

In the 20th century discoveries in condensed matter physics enabled significant technological advancements. The development of the band theory of solids by the 1930s successfully explained the conduction and optical properties of most materials known at the time. Extensive research into the properties of semiconductors allowed John Bardeen, Walter Brattain, and William Shockley to invent the transistor [1], which subsequently drove the computer era. Other semiconductor based technologies such as digital cameras and solar cells also relied on the success of band theory. However, band theory could not explain superconductivity, a phase of matter that has zero electrical resistance and completely expels magnetic flux below a critical temperature, which had been known since 1911 [2]. Even before a microscopic theory of superconductivity was completed, superconducting electromagnets were being developed. In 1957, John Bardeen along with Cooper and Schrieffer developed a theory of superconductivity [3] which was thought to describe all known superconductors at the time, which were elemental metals and simple metal alloys. Despite the extreme cryogenic requirements for superconductivity to emerge, these early superconducting materials have found applications in medical imaging and various scientific instrumentation.

In the 1980's, the discovery of superconductivity in materials containing copper oxide layers called cuprates changed the field of condensed matter physics [4]. These superconductors come from compounds that are not good metals and for several compounds superconductivity appears at temperatures above the boiling point of nitrogen [5]. From a technological standpoint, these materials brought hopes of superconducting technologies that do not need limited and expensive liquid helium. Of course, this also created a drive to find a room

temperature, ambient pressure superconductor- a goal that has not yet been realized. High-temperature superconductors are now being used in superconducting magnets to achieve higher critical fields for scientific purposes, such as a 32 Tesla all-superconducting magnet for high-field experiments at the National High Magnetic Field Laboratory [6]. The discovery of superconductivity in the cuprates also re-energized the field from a basic science perspective because the new superconductors could not be explained by the theory of Bardeen, Cooper, and Schrieffer (BCS), and are called unconventional for this reason. While this paradigm shift was foreshadowed years earlier by the discovery of superconductivity in heavy fermion materials, whose magnetic ions should preclude superconductivity [7], cuprates were the catalyst for many new thrusts into unconventional superconductivity.

Aside from superconductivity that cannot be explained by BCS theory, cuprates turned out to host several other emergent phenomena in the vicinity of superconductivity [8, 9, 10, 11]. Using tuning parameters such doping or temperature, one can access phases like antiferromagnetim, an unusual pseudogap phase, nematicity, and charge order. Electron interactions must be considered to explain any of these broken-symmetry states [12]. Additionally, the problem is no longer explaining any individual phase, but also how it fits in with its neighboring phases. It turns out this is quite difficult because all of these phases interact with one another in complicated and surprising ways; you cannot alter one without affecting the others [13]. One chapter of this work will focus on the charge order in a cuprate superconductor and how it couples to the lattice. A key take away will be that the relationship between charge order and the lattice cannot be understood without also considering the effects of other phases, such as superconductivity.

The next class of unconventional superconductors to rival the cuprates in diversity of materials and phases are the iron-based superconductors. Their unifying structural motif is a square layer of iron with a pnictogen (Pn) or chalcogen (Ch) tetrahedrally situated above and below [14]. While not exhibiting superconducting transition temperatures as high as in the cuprates, the iron-based superconductors can still achieve transition temperatures much

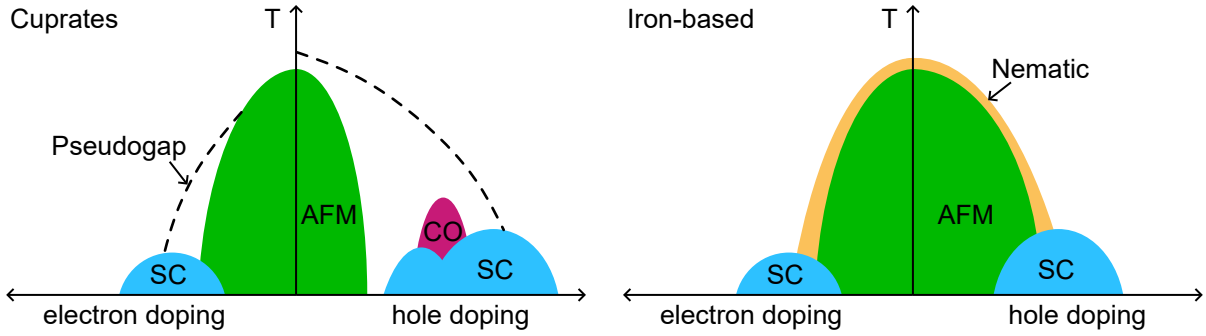

Figure 1.1: Schematic phase diagram of cuprates and iron-based superconductors showing Temperature v.s. electron and hole doping.

higher than in BCS superconductors. It also turns out that their transition temperatures can be highly tunable with both chemical doping and mechanical pressure [15]. These tuning parameters can also access other neighboring exotic states, such as an antiferromagnetic ground state (for most iron-based superconductors) and nematicity. The nematic state has been a large focus in iron-based superconductors because of its universality, likely correlated electron origin, and deep connection with the superconductivity [16, 17]. Comparisons are often drawn between the structure and phase diagrams of iron-pnictides and the cuprates [18]. Structurally, both classes are made up of layers of square lattices containing their titular element, Fe or Cu. For the cuprates, the Cu-O layers are considered critical to the superconductivity, and in the iron-based superconductors it is the Fe-Pn/Fe-Ch layers [19]. In their phase diagrams, both groups have a superconducting dome in both the electron and hole-doped sides and an antiferromagnetic ground state in the parent compound, see Fig. 1.1. However, there are some marked differences: the parent compounds of the cuprates are Mott insulators, but are correlated metals for iron-based superconductors, and there is no known charge order in the iron-based superconductors [18]. Additionally, not all iron-based superconductors follow the above phase diagram. The iron-chalcogenides have no magnetic ground state at ambient pressure, and in some cases the parent compound itself is a superconductor [20].

The chalcogenides present their own set of unique opportunities. In this class of iron-

based superconductors, isovalent chemical substitution are typically used to tune the material rather than electron or hole doping [21]. In systems containing tellurium there is evidence of topologically non-trivial band structures [22]. The Fe(Se, S) system likely hosts two distinct superconducting states on either side of the nematic phase transition [23]. The bulk of this work will focus on the detection of an electronic state near the Fermi level breaking both translational and rotational symmetry in $FeSe_{1-x}S_x$.

Before discussing the projects I have worked on, I will describe the experimental techniques used and give a background on the materials studied. The experimental techniques section will cover scanning tunneling microscopy/spectroscopy (STM/S), angle-resolved photoemission spectroscopy, and resonant x-ray scattering. The material background will focus on the phases most relevant to this work: nematicity, superconductivity, and charge order. The emphasis will be on $FeSe_{1-x}S_x$, so a discussion of magnetism will be omitted, but a discussion of charge order is included due to its importance for $La_{1.475}Nd_{0.4}Sr_{0.125}CuO_4$. Chapters 4 and 5 will present the primary projects I have worked on: scanning tunneling microscopy studies on $FeSe_{0.81}S_{0.19}$ and probing charge order in $La_{1.475}Nd_{0.4}Sr_{0.125}CuO_4$ using resonant x-ray scattering, which are published in npj Quantum Materials and Physical Review Research, respectively.

Chapter 2

Overview of Experimental Techniques

The experimental results in Chapter 4 were done using scanning tunneling microscopy/spectroscopy (STM/S), with an emphasis on the spectroscopy. To assist in the interpretation of these results, angle-resolved photoemission spectroscopy (ARPES) experiments were also performed. The two techniques are good complimentary probes of the electronic states. Even though STM/S will play a larger role in this work, the ARPES technique will be introduced first as an understanding of ARPES will help in understanding the spectroscopy aspect of STM/S. Afterwards some experimental advantages/weaknesses and technical requirements for the two techniques will be compared. Finally, I will describe resonant x-ray scattering which I used in Chapter 5. Much of the description of ARPES is based on a review by Prof. Andrea Damascelli [24]. The section on tunneling spectroscopy and quasiparticle interference is based on a review by Prof. Ali Yazdani et. al. [25]. The overview of resonant x-ray scattering follows a review by Prof. Riccardo Comin et. al. [26].

The STM/S experiments were all carried out on a commericially available Unisoku USM 1300 STM. The ARPES was performed at the Canadian Lightsource at the new QMSC beamline. The resonant x-ray scattering experiments were done across several beamlines at both the Canadian Lightsource and BESSY-II. I will describe some relevant specifics of these instruments.

2.1 Angle-Resolved Photoemission Spectroscopy

Angle-Resolved Photoemission Spectroscopy (ARPES) is a photon-in, electron-out technique that leverages the photoelectric effect to probe the energy/momentum dispersion relation of

electrons near the surface in a metal or semi-metal. High intensity, monochromatic light is shined at the surface of the sample at a particular incident angle. If the energy of the photons is greater than the work function of the sample, electrons near the surface can be ejected into the vacuum. Due to energy and momentum conservation laws, these photoelectrons retain information of the binding energy and crystal momentum they had while living in the lattice environment. After ejection, the photoelectrons pass through an analyzer that spatially separates them by energy and exit angle. The electrons are then counted using a two-dimensional electron detector, such as a microchannel plate, which can then be used to illuminate a charge-coupled device (CCD). The position on the CCD can be mapped to an emission angle, which can be used to calculate the initial energy and momentum of the electron inside the crystal. For a single photon incident angle, an ARPES image only tells you about the in-plane momentum in one direction. However, if you vary the angle of incidence of the light, you can access more in-plane momentum directions. In this way you can construct a map of the band structure for all in-plane momentum directions.

The physical quantities measured during an ARPES experiment are the kinetic energy of an outgoing photoelectron, E_{kin} and the angles that it exited the sample with, θ, φ. These quantities can be related to the desired sample quantities, the binding energy and in-plane crystal momentum of the surface electrons, E_{b} and $\mathbf{k}_{||}$ with the following conservation of energy and momentum equations:

$$E_{\text{kin}} = h\nu - \phi - |E_{\text{b}}| \tag{2.1}$$

$$\mathbf{k}_{||} = \frac{1}{\hbar}\sqrt{2mE_{\text{kin}}}\sin\theta, \tag{2.2}$$

where ϕ is the work function of the material and ν is the frequency of the incident light. Thus a dispersion relation between the binding energy and in-plane crystal momentum of the surface electrons can be reconstructed. While the out-of-plane momentum is not strictly conserved, if one approximates the states after photoemission to be that of nearly-free electron,

information about $\mathbf{k}_\perp$ can be extracted from

$$\mathbf{k}_\perp = \frac{1}{\hbar}\sqrt{2m(E_{\text{kin}}\cos^2\theta + V_0)}\,, \tag{2.3}$$

where V_0 is the offset between the bottom of the valance band and the vacuum energy. So by varying the incoming photon energy, and therefore varying E_{kin}, the $\mathbf{k}_\text{z}$ dispersion can be determined. The intensity measured by an ARPES experiment is

$$I(\mathbf{k},\omega) = I_0(\mathbf{k},\nu,\mathbf{A})f(\omega)\mathbf{A}(\mathbf{k},\omega) \tag{2.4}$$

where I_0 is related to transition matrix elements, $f(\omega)$ is the Fermi-Dirac cutoff, and $\mathbf{A}$ is the single particle spectral function. The Fermi-Dirac cutoff comes into play because ARPES can only measure occupied states. The matrix elements just capture the fact that some transitions are less probable than others, but the experimental effect can be complicated. The spectral function includes the single particle band structures as well as captures the effects of interactions.

Experimental considerations

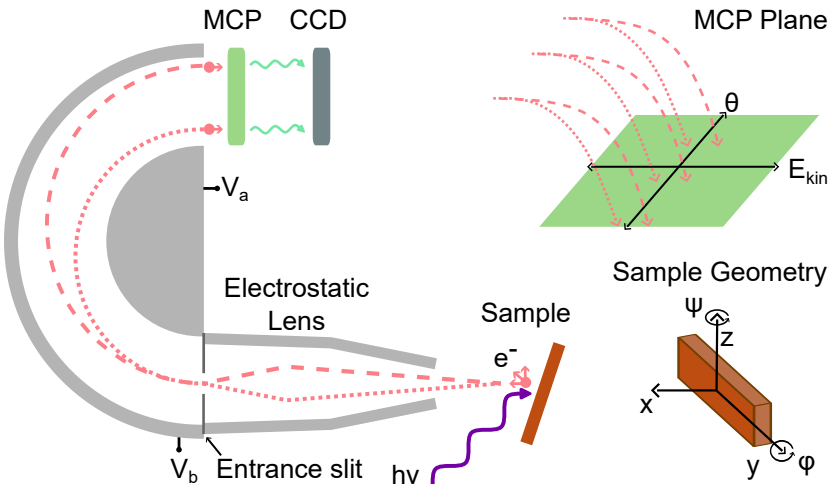

Figure 2.1: A schematic diagram of an ARPES experimental setup. V_a and V_b label the voltages applied to the two hemispheres. The sample geometry labels the two sample angles θ and φ used in this work. The MCP plane shows how the electrons of different energy and emission angle are projected onto the surface of the two-dimensional MCP.

The ARPES experiments in this work were performed using light produced by a synchrotron, which produces highly intense and monochromatic light whose wavelength is highly tunable. Figure 2.1 shows a schematic cutout of a hemispherical analyzer within an ARPES experimental setup. Light hits the sample surface and causes the ejection of photoelectrons in all directions away from the sample. The electrostatic lens focuses the electrons toward the entrance slit, which only accepts electrons within a finite emission angle and a narrow energy range. The long axis of the entrance slit can be oriented parallel or perpendicular to the slit-detector direction; this schematic shows a perpendicular slit. The two hemispheres are held at different voltages (V_a and V_b) which deflects the path of the electrons depending on their kinetic energy. A two-dimensional microchannel plate (MCP) sits on the other side of the analyzer to amplify the number of electrons and fluoresce onto a CCD. The two-dimensional nature of the MCP and the CCD preserves both the kinetic energy and emission angle information of the electrons. The range of kinetic energy and emission angles measured are determined by the entrance slit. A single ARPES image will provide the single particle spectral function as a function of binding energy and a particular in-plane momentum direction. Typically samples will be oriented so that normal emission accesses a high-symmetry point of the Brillouin zone, most commonly the zone center. The sample angle ψ can be rotated to center the feature-of-interest on the detector. The sample angle φ can be rotated to access momenta in the direction orthogonal to ψ. If images are taken for a series of φ values, one can map out constant energy contours (including the Fermi surface). Images are typically analyzed with energy distribution curves (EDCS), or momentum distribution curves (MDCS), which are line cuts taken at constant momentum or energy, respectively.

Resolution, Calibration, and Systematics

The energy resolution of a measurement is determined by a combination of beamline and analyzer settings. The momentum resolution is determined by the photon energy and analyzer settings. From Eq. 2.3, lower photon energies correspond to higher momentum resolution, but sacrifice intensity. On matrix element effects, important considerations are scattering

geometry, orbital character of the bands being measured, and polarization of the incident light. The binding energy of the electrons is usually plotted relative to the Fermi level of the system, which has to be determined. The analyzer energy can be calibrated by determining the Fermi level on a spectra from a known material, such as a gold wire. The Fermi level is determined by fitting EDCs to a finite-temperature Fermi-Dirac function. The Fermi level should be featureless across θ values, but projecting a three-dimensional curved path onto two-dimensional surface will cause the Fermi level to appear curved. The same spectra can be used to perform corrections in the projection of the energies due to slit geometry.

2.2 Scanning Tunneling Microscopy/Spectroscopy

Binnig and Rohher first reported their successful atomic scale images from their scanning tunneling microscope in 1982 [27] and later shared the Nobel Prize for their invention in 1986. Scanning tunneling microscopy (STM) uses the phenomenon of quantum tunneling to image the surface of samples with atomic resolution. A sharp metallic tip is brought very close to a sample surface, usually within a few angstroms, and a voltage difference is applied between the tip and the sample. If the tip is close enough electrons can tunnel from the tip to the sample, or vice versa, establishing a tunneling current. The tip is scanned across the surface of the sample and kept at the same height, the tunneling current will vary based on the number of electrons available to tunnel. Alternatively, a feedback loop can be set up to enforce a constant tunneling current by allowing the tip height to vary as it is scanned along the surface. If the tip is scanned across a two-dimensional grid, recording the height of the tip needed to maintain the desired current at each position, one can obtain an image of the surface of the material, known as a topography. Important information can be afforded by topographies, such as atomic spacing, the presence of surface reconstructions or defects, and more. However this work will focus on another mode of measurement possible with STMs: spectroscopy.

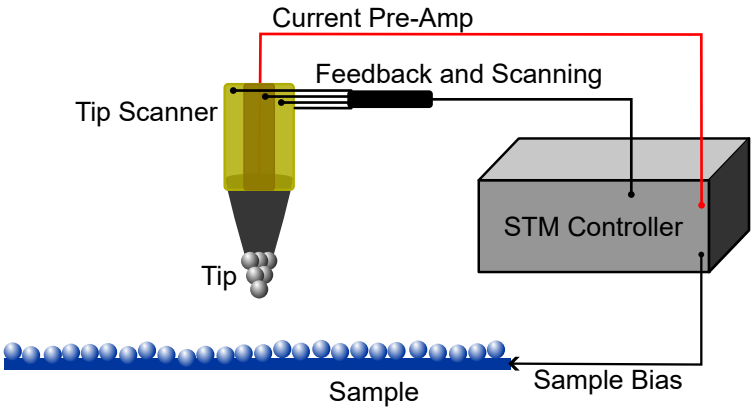

Figure 2.2: Schematic diagram of an STM/S experimental setup.

Spectroscopy

Tunneling spectroscopy can extract information about about the electronic density of states, including direct measurement of superconducting gap properties. Adding spatial resolution, one can reconstruct details of the energy and momentum dependent band structure. From the probability of a transition of electron from the sample to the tip and using after a low temperature and low voltage approximation that turns the Fermi functions into step functions, the tunneling current is given by

$$I(V) = \frac{2\pi e}{\hbar} \int_0^{eV} \rho_s(E_F - eV + \epsilon)\ \rho_t(E_F + \epsilon)\ |M|^2\ d\epsilon, \tag{2.5}$$

where V is the voltage applied, M is the transition matrix elements, and $\rho(E)$ is a density of states. If the tip is a metal, its density of states near the Fermi level is a constant. Using this approximation and taking the derivative of both sides, Tersoff and Hamman [28] determined that

$$\frac{dI(V)}{dV} \propto \rho_s(E_F - eV). \tag{2.6}$$

Thus, the density of states of the sample for a given energy is proportional to the differential conductance, or dI/dV.

One can measure the differential conductance in two ways: (i) measure $I(V)$ and numerically integrate it or (ii) directly measure the differential conductance by releasing the feedback control to keep the tip-sample distance mixed and then sweeping the applied bias and measuring the response in current using a lock-in amplifier. In this work, all measurements of dI/dV are done using the lock-in technique.

While Eq. 2.5 does not explicitly show any spatial dependence, the density of states for any real material is of course spatially varying (called local density of states, or LDOS). To take a dI/dV map, one first sets up a predetermined grid of points (256x256 is a standard in the field) and measure the dI/dV at each of these points. While moving the tip between points in the grid, the feedback is turned back on to keep the set-point current. Typically, a topography is also recorded while the feedback is on.

Quasiparticle Interference

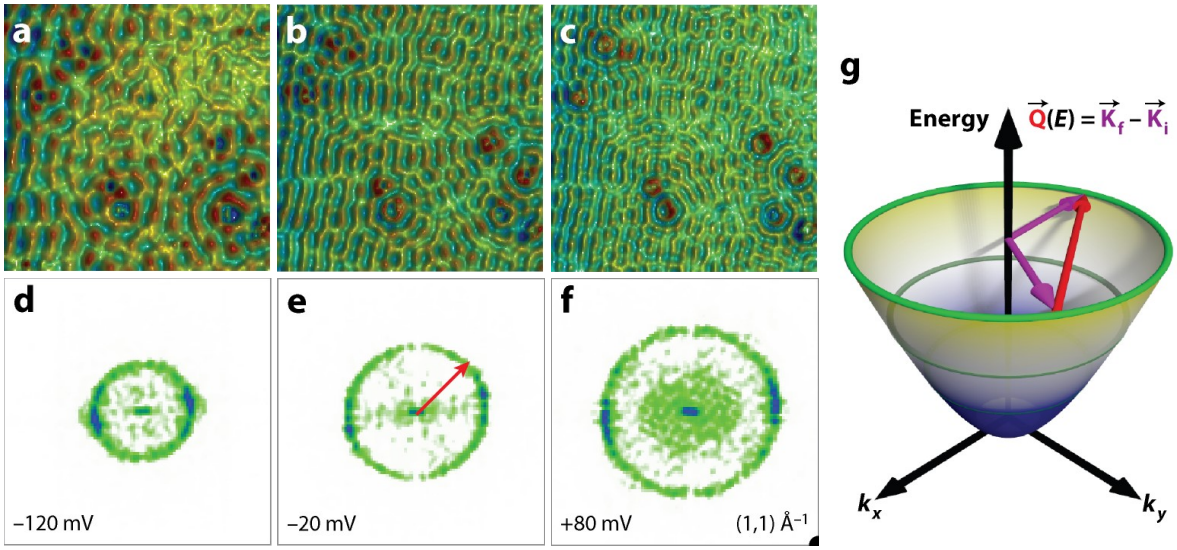

Figure 2.3: Demonstration of QPI on Cu (111). **a-c** dI/dV maps on Cu (111) showing QPI patterns for different energy cuts. **d-f** FFTs of **a-c**. **g** Schematic of the band structure of Cu (111) showing the scattered wave vector across a constant energy contour. All panels reproduced from [25].

The wavefunctions for electrons in a periodic potential (lattice) are Bloch wavefunctions of the form $\psi(\mathbf{r}) = u(\mathbf{r})e^{i\mathbf{k}\cdot\mathbf{r}}$. The LDOS will be uniform in this case because there is only one wavevector. If this wavefunction encounters a defect, it will see a different potential that

disrupts the periodicity of the lattice, causing it to scatter. After scattering, the wavevector $\mathbf{k}$, is modified. Now there is more than one wavevector present and can interfere with one another creating interference patterns known as quasiparticle interference (QPI). If these interference patterns are Fourier transformed into reciprocal space, the peaks will occur at wavevectors $\mathbf{q} = \mathbf{k}_\mathrm{f} - \mathbf{k}_\mathrm{i}$, where $\mathbf{k}_\mathrm{f}$ and $\mathbf{k}_\mathrm{i}$ are the final wavevector after the scattering and the initial wavevector, respectively. For a given energy (applied bias), both the initial and final wavevectors must lie on a constant energy contour allowed by the band structure. By exploiting the $\mathbf{k}$-space symmetry of the band structure, one can reconstruct the band structure in $\mathbf{k}$-space from the measured bands in $\mathbf{q}$-space. To do this, some knowledge of the band structure and its projection onto the surface is required, commonly from ARPES or DFT calculations [25].

The Cu (111) surface offeres a prototypical example of using QPI to reconstruct band structure because it has a very simple, round Fermi surface with nearly parabolic bands. This is useful for understanding how the band structure reconstruction is done using a simple case, before attempting to perform it on multi-band systems that are studied in this work. Figure 2.3 shows the differential conductance on the surface of Cu (111) at several energy cuts to demonstrate the evolution of QPI as a function of energy. As the energy increases the wavelength of the QPI patterns decreases. This is also observable in Fourier space (Fig. 2.3d-f, where the peaks move to larger $\mathbf{q}$ values as energy increases. These observations can be explained by the upward parabolic dispersion of the single band shown in Fig. 2.3g.

About the Unisoku 1300 STM

The STM head has the tip stage farthest down so the tip would be pointing upward, and the sample stage above it, with the sample face down. The sample stage is moved with coarse piezo motors which can be used when the tip is outside of tunneling range to make large movements in x and y. The tip stage has two sets of piezo motors; the scan stage can be moved with fine piezo motors which are used for scanning and tip height control while tunneling, and the approach stage is used to move the tip close to within tunneling range of

the sample. The approach stage uses an inertial piezo slider, or a slip-stick motor, to make large, coarse motions. The scanning stage is made of a tube-type piezo. A downside of the tube-type piezo is that the x and y directions are coupled, and for large voltages the motion can be non-linear. Scan control software can account for the coupled motion, but one must be careful of the non-linear behaviour. This is best combated by choosing to keep scans near the center of the piezo range where linearity is preserved. If this cannot be accomplished due to experimental constraints, corrections can be applied during analysis, such as subtracting a parabolic background. This model has a 60 L tank for liquid helium which will keep a sample at 4.2 K for about 5.5 days before the tank needs to be refilled with helium.

Spatial calibration

The piezoelectric effect is temperature dependent, so the STM manufacturer performed applied voltage to distance calibrations at the factory for three temperatures. However, we also performed calibrations on the sample of interest after final installation. The spatial calibration is done by measuring the atomic spacing of a sample whose atomic spacing is well-known. This is best done using the Fourier transform of an atomic resolution image and performing the calibration in **k**-space. All results in this work have been calibrated in this way.

Sample Preparation

In order to truly measure the electronic properties of the sample, the surface must be free from surface contamination and to prevent the tip from contacting the surface it must atomically level. To achieve this, samples are either cleaved or sputtered and annealed in an ultra-high vacuum (UHV) environment that is connected to the STM head so that the sample remains in vacuum after treatment. For cleaving *in situ*, an inert cylindrical object (top post) is glued on the sample surface before it in inserted in the UHV system. The top post is then mechanically removed inside the UHV environment, taking with it the top few layers of the sample. What remains should be a clean surface that has never been exposed to atmosphere. Before insertion into the STM head, the cleaved sample is visually inspected

through a window to ensure that the entire sample was not removed during the cleave and that excess glue was not left behind. For highly laminate materials like FeSe, another concern is that the top surface has "flakes". Flakes will cause problems for the tip because they can extend several microns above the actual sample surface, increasing the likelihood of a crash, they can have an extremely sloped surface that cannot be corrected for with the scanning algorithm, and they can have poor electrical connection. There is not real science behind what will lead to a good cleave, but some factors that impact the cleave are initial sample condition, amount of glue used in mounting the sample, size of the post relative to the sample, and amount of glue used on the post. Specifically, for FeSe the initial sample condition is highly relevant. Since these samples are air sensitive, their surfaces can become highly oxidized. While the cleave should be able to remove the oxide layers, samples that have experienced significant exposure to atmosphere can have degradation beyond the surface. The layers of material start to peel away from each other, like a book that has gotten wet and then dried again. When this happens the oxidation can start to affect the interior layers of the sample.

Comparison of STM/S and ARPES

ARPES and STM/S have similar requirements for the sample environment. Because ARPES is a surface sensitive technique, samples are usually cleaved *in situ* in a UHV environment of $1x10^{-10}$ torr or better. Samples must have a good electrical connection to ground to prevent charging due to photoemission. However, the cryogenic requirements are different between ARPES and STM. The geometry of an ARPES experiment does not easily allow for the use of a bath cryostat, so the base temperature of an ARPES experiment is typically around 10 K.

There are several experimental advantages afforded by combining STM/S with ARPES over ARPES alone. For one, essentially the only limit on energy resolution in STS measurements is temperature, and many STM/S instruments can be taken to sub-Kelvin temperatures. Momentum resolution can also match that of ARPES by taking larger spatial maps.

Also, one can perform STS measurements under high magnetic field, while ARPES cannot be done in the presence of magnetic fields. Finally, STS measurements are not restricted to only occupied states.

2.3 Resonant X-ray Scattering

Resonant x-ray scattering is a photon-in photon-out used to study the electronic states of crystalline materials. Traditional x-ray scattering techniques, like Laue or x-ray diffraction, use the interaction of light with the electrons surrounding atomic nuclei to probe the crystal structure and chemical composition of materials. Resonant x-ray scattering is potentially sensitive to much weaker, periodic electronic modulations. In particular, it has been widely used to study the charge ordering phenomena in the cuprates. It is a bulk probe, making it a good complement to surface techniques like STM/S and ARPES.

In a traditional reflection geometry experiment, incoming photons of momentum $\mathbf{k}_\mathrm{i}$ incident at angle θ scatter off of the electrons in the sample, which impart some momentum transfer $\mathbf{Q}$, leaving the exiting photons with momentum $\mathbf{k}_\mathrm{f}$. These momenta are related by $\mathbf{Q} = \mathbf{k}_\mathrm{f} - \mathbf{k}_\mathrm{i}$. A detector is placed at an angle 2θ (not necessarily equal to $2^*\theta$) to count the number of outgoing photons at that angle. The sample angle can be swept to map this out for various $\mathbf{Q}$ values.

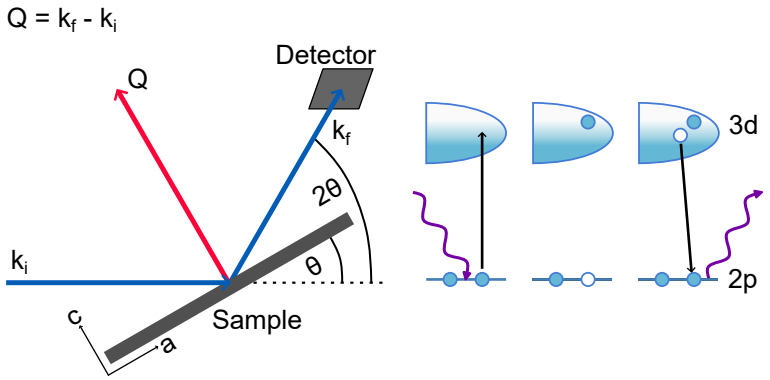

Figure 2.4: A schematic diagram of an x-ray scattering geometry.

Figure 2.4 shows a simple scattering geometry where the sample is oriented such that

$\mathbf{Q}||$c, so excitations in the [0 0 L] directions will be probed. In this particular case, $\theta = 2\theta$, but to probe any in-plane momenta, $2\theta \neq \theta$.

Resonant x-ray scattering is similar in operation, except the incoming photon energy is tuned to the absorption energy of particular electrons. In this case the incoming photon excites a core electron to the conduction band, and another electron relaxes back down to the now unoccupied core state, emitting a photon. The photon of course has to experience the same momentum transfer as in the non-resonant case, preserving the scattering component of the experiment. However, now a higher percentage of the outgoing photons will have participated in the absorption process, thus the experiment is probing primarily the intermediate state electrons. Because the absorption energy is dependent on the element and the final and initial states of the electrons involved, resonant x-ray scattering is both element and orbital specific. The detection of the exiting photons can be done with an energy-integrating detector, or an energy-resolving detector. Experiments done using the latter are called resonant inelastic x-ray scattering (RIXS). In a RIXS experiment, the outgoing x-rays are sent through a spectrometer that separates them by energy before counting them with a two-dimensional detector (CCD). This allows the tracking of photon energy loss and momentum transfer. The photon energy loss may be due to several phenomena, such as absorption due to a phonon, magnon, or other collective excitation. The largest signal in a RIXS experiment occurs at E_{loss}=0, which is known as the elastic line.

Experimental considerations

Most resonant x-ray scattering experiments can measure the flow of charge due to photoabsorption, known as the total electron yield (TEY). This is often a helpful technique for finding and aligning samples because it does not depend on precise detector positioning. It is also commonly used for absorption spectroscopy, although there are known saturation effects. Another method for accomplishing the same goals in measuring the fluorescence at normal incidence using a photon detector, called total fluorescence yield (TFY). While slightly more difficult due to needing to align the detector, TFY can be more reliable and can give more

information about the surface quality. The absorption edges used in this work with be the Cu-L_3 edge, the O-K edge, and the Fe-L edge, which are all within the soft x-ray regime. This means a need for ultra-high vacuum, as soft x-rays do not penetrate air, and either a cleaved or polished sample surface, as soft x-rays have slight surface sensitivity. In order to know what momentum states are being accessed, samples have to be precisely aligned before beginning an x-ray scattering experiment. At quasi-elastic scattering beamlines, a few Bragg peaks can typically be accessed so there is room for some *in situ* alignment. But for inelastic scattering beamlines, photon energies are usually capped below what is needed to access any in-plane Bragg peaks.

Chapter 3

Background of Materials Studied

In this chapter I will cover the basic properties of the primary material studied in this work, $FeSe_{1-x}S_x$. Then I will discuss the phases that are most relevant to this material; nematicity and superconductivity. In each section, I will start with a general description of what the phase is followed with how they manifest in $FeSe_{1-x}S_x$. Finally, I will discuss charge order, which is not usually discussed in regard to iron-based superconductors, but is extremely relevant to cuprate superconductors and therefore Chapter 5. In this section I will primarily discuss how charge order manifests in the cuprates.

3.1 Basic properties of $FeSe_{1-x}S_x$

There are many great review articles on the topic of $FeSe_{1-x}S_x$ and iron-based superconductors in general. Perhaps the most useful and relevant reviews to this work are by Professor Amalia Coldea [21] and two reviews be Anna Bohmer et. al. [29, 30], and significant portions of this chapter follow these reviews. Others helpful works include a review on unconventional superconductivity by Professor Greg Stewart [31] and a review of exotic superconducting states by Prof. Shibauchi et. al. [32].

The $FeSe_{1-x}S_x$ system provides a convenient canvas for studying the interplay between ordered states in an iron-based superconductor as it has no magnetic ground state at ambient pressure, leaving only the superconductivity and nematicity to contend with. There is an electronic nematic transition at 90 K which persists through a superconducting transition at 8 K, see Fig. 3.1a [33, 21]. Sulfur substitution for selenium has been shown to significantly alter the nematicity without introducing long-range magnetic order and only moderately

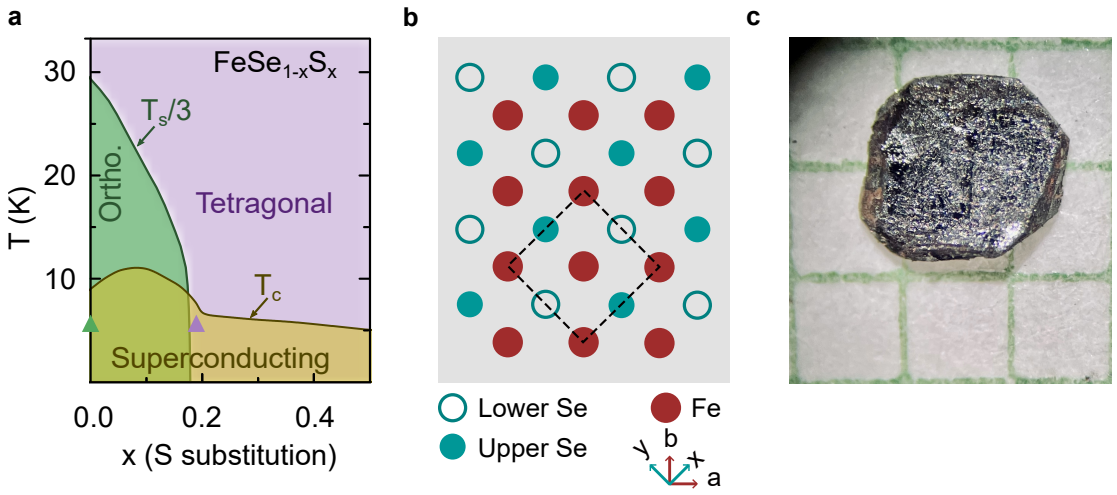

Figure 3.1: **a** Phase diagram of $FeSe_{1-x}S_x$ based on [21], indicating the structural and superconducting transitions, T_S and T_c. For simplicity, we show the $T_S/3$ line. The two samples studied in this work ($x = 0$ and $x = 0.19$) were measured at 4.2 K, green and purple triangles, respectively. **b** Schematic of the crystal structure of pure FeSe. Red circles are top layer Fe, turquoise circles are top layer Se, and turquoise open circles are Se in the layer below. Arrows labeled a and b indicate the shortest Fe-Fe bond direction, and arrows labeled x and y indicate the shortest Se-Se bond direction. **c** Image of $FeSe_{0.81}S_{0.19}$ on graph paper with grid size of 1 mm x 1 mm.

altering T_c[20]. There is a proposed nematic quantum critical point near $x = 0.17$, where the nematic transition is suppressed to 0 K. At the same sulfur concentration the superconducting T_c drops to a minimum of 4 K, but persists to FeS [34]. Thus, sulfur substitution is a great tuning parameter to explore the relationship between superconductivity and nematicity without the complication of long-range magnetism.

The crystal structure of FeSe is quite simple: alternating layers of square Fe and square Se lattices where the Se atoms form distorted tetrahedra above/below the Fe plane. A 2D projection of the FeSe crystal structure in shown in Fig. 3.1b. In this work, a,b will refer to the shortest Fe-Fe bond direction, and x,y will refer to the shortest Se-Se bond direction. In $FeSe_{1-x}S_x$, smaller S atoms randomly replace Se atoms, which is an isovalent substitution. $FeSe_{1-x}S_x$ crystals grow as 1-2 mm sized platelets that are black and shiny in appearance, see Fig. 3.1c. They are highly sensitive to oxidation and must be stored in an inert environment. However, due to their quasi-two dimensional structure, weak van der Waal's forces between

layers make them easy to cleave. At room temperature the lattice parameters of FeSe are $a = 3.7651$ Å and $c = 5.0301$ Å, and for the sulfur concentrations relevant to this work the a axis changes by less than 2% according to Vergard's law[21].

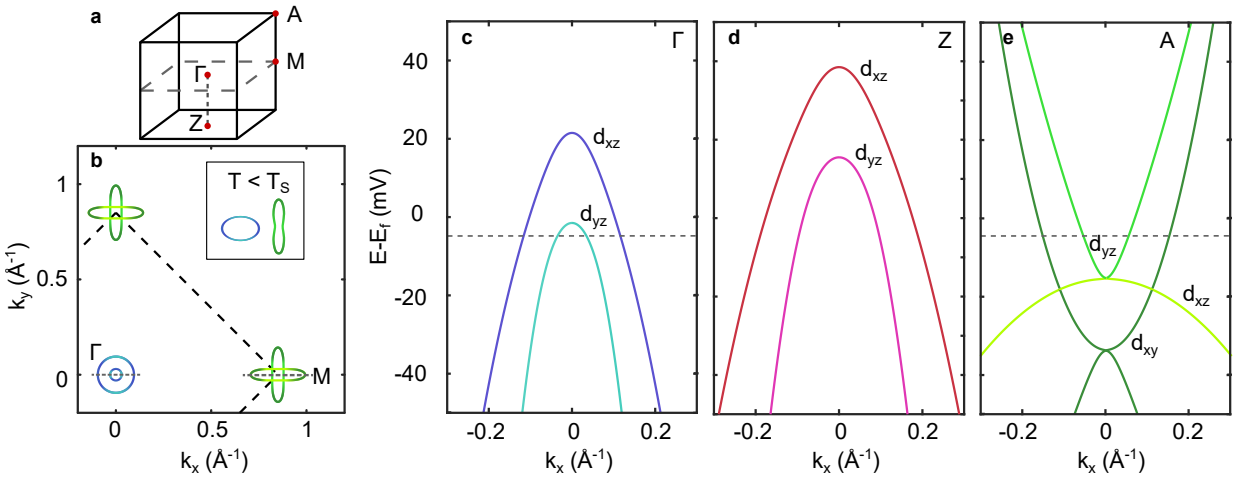

Figure 3.2: **a** Schematic of the Brillouin zone for $FeSe_{1-x}S_x$ using a two-iron unit cell labeling the relevant high symmetry points. **b** Schematic constant-energy contour of tetragonal $FeSe_{1-x}S_x$ with $k_z = 0$. The colors indicate the primary orbital character of the states, which are labeled in **c-e**. The black dashed indicate the the two-iron unit cell. The grey dashed lines indicate the direction of the cuts taken in **c-e**. The inset shows the shape of the pockets in the nematic state. **c-e** Schematic band structure of tetragonal $FeSe_{1-x}S_x$ at the labeled high-symmetry points. The grey dashed lines indicate the approximate energy level of the constant energy contours in **b**.

The low-energy electronic states of iron-based superconductors comes from a Fe^{2+} which has a $^3d_6$ electronic configuration. This means that for $FeSe_{1-x}S_x$, all 5 Fe d-orbitals are potentially relevant to the low-energy states. Fortunately, in the crystalline environment the degeneracy of these orbitals is lifted, but because of the distorted tetrahedral environment, it turns out all 5 orbitals remain near the Fermi energy. In particular, the d_{xy}, d_{xz}, and d_{yz} orbitals are nearly degenerate and are closest to the Fermi level[19]. Figure 3.2 summarizes the electronic states of tetragonal $FeSe_{1-x}S_x$ in **k**-space. The relevant high symmetry points to the electronic states are the Γ, Z, M and A points whose locations are indicated in Fig. 3.2a. Constant-energy cuts of the electronic structure consists of two concentric hole-like pockets at the Brillouin zone center and two crossed ovoid electron-like pockets at the zone corners, see Fig. 3.2b. Along the direction indicated by the dashed grey lines, the outer hole pocket

at Γ, Z has primarily d_{xz} orbital character while the inner pocket has primarily d_{yz} orbital character. The dominant orbital character is flipped when taking the cut perpendicular to the direction shown. At the corners, the high curvature ends of the ovals have primarily d_{xy} orbital character, while the nearly flat sides of the ovals have either d_{xz} or d_{yz} character. For the flat side in the constant-**k** cut shown, the orbital character is primarily d_{yz}. Below the Fermi level when this pocket becomes hole-like, the orbital character is swapped. The hole pockets at the center exhibit strong k_z dependence while the pockets at the corners are nearly two-dimensional.

3.2 Nematicity

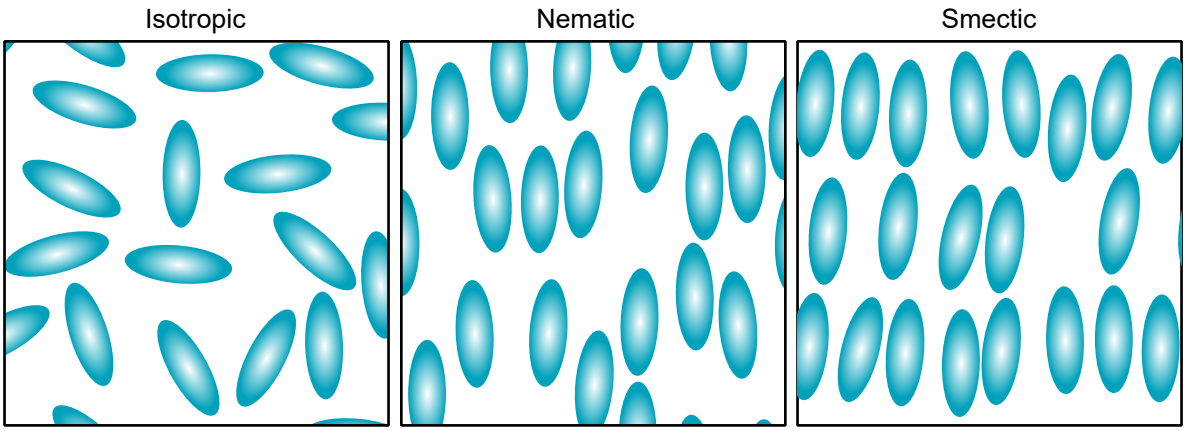

Figure 3.3: Schematic drawing showing the difference between isotropic, nematic, and smectic phases.

Used in the original context of liquid crystals, nematicity refers to molecules breaking rotational symmetry by having a preferred orientation without breaking translational symmetry. In a crystalline solid, nematicity is when electronic correlations cause discrete rotational symmetry breaking without any additional symmetry breaking. In the iron-based superconductors, this rotational symmetry breaking is observed in the Fe-plane when the electronic states near the Fermi level along the two Fe-Fe bond directions become inequivalent. The

lattice also breaks rotational symmetry in the form of a tetragonal to orthorhombic distortion. For most iron-based superconductors, spin degrees of freedom also break rotational symmetry near the former transitions. Whether spin, charge, or lattice degrees of freedom are primarily responsible for driving nematic state is a difficult question because all three symmetry breaking phenomena occur at once. However, extensive experimental evidence and theoretical work have led the community to conclude that low-energy electronic correlations are responsible [16]. For example, the measured anisotropies in resistivity, optical conductivity, and magnetic susceptibility are significantly larger than they should be if they were caused by the small lattice distortions alone [35, 36, 37, 38].

The effects of nematicity in iron-based superconductors were first observed as a structural tetragonal to orthorhombic transition at the structural/nematic transition temperature, T_S. In $FeSe_{1-x}S_x$, T_S is around 90 K. At 5 K, well below T_S, the lattice parameters a and b are no longer equivalent (a = 3.753 Å, b = 3.772 Å) whereas at room temperature a = b = 3.774 Å [39]. The structural transition can be detected in transport measurements as a kink in the in-plane resistivity or an anomaly in magnetic susceptibility, and a second order phase transition is evident in heat capacity measurements [40, 41, 42]. Nematicity also shows up as an anisotropy in the in-plane resistivity. The nematic susceptibility can be determined by elasto-resistance measurements where the resistivity is measured before and after applying a small strain to determine $\Delta R/R$, which is proportional to the nematic order parameter[43, 20]. In $FeSe_{1-x}S_x$ the nematic susceptibility diverges near x_c, leading to claims of a nematic quantum critical point in this system[20]. In regimes where nematic susceptibility is large, small amounts of strain could create dramatic changes to the nematicity.

The electronic states become anisotropic in the nematic state. ARPES measurements have revealed the circular hole pockets at the zone centers become elliptical with the semi-major axis pointing along the Fe-Fe bond direction while the electron pockets at the corners become peanut shaped [44] (see inset of Fig. 3.2b). Measurements on detwinned FeSe crystals show that the d_{xy} band at the M point actually disappears [45]. One explanation for

the "missing" electron pocket that the electron pocket is pushed above the Fermi level after undergoing a Lifshitz transition [46, 47]. Another manifestation of nematicity is orbital-ordering, where electrons preferentially occupy particular d-orbitals over others, further lifting the degeneracy of the involved bands. After the nematic transition the d_{xz}, d_{yz}, and d_{xy} bands further separate in energy. The magnitude of this separation known as the nematic energy scale, and its momentum dependence can help narrow down viable nematic order parameters. The nematic energy scale at the zone center is of order 10 meV, and while the separation of electron bands the zone corners is about 50 meV, there is some debate whether the separation is solely due to nematicity [48]. Chemical pressure by S substitution suppresses the orbital ordering in a similar way to increasing temperature [49].

There are many open questions about the nematic state, particularly whether spin or charge/orbital fluctuations are responsible for driving it [29]. This has been particularly difficult to answer because there may not be a single answer for all classes of iron-based superconductors. For example, iron-pnictides develop antiferromagnetic order near the nematic transition, making a spin fluctuation scenario plausible. However, in chalcogenides no long-range magnetic order ever stabilizes at ambient pressure. Magnetic fluctuations are present in this system, and physical pressure does act to pin the fluctuations, so a spin origin of the nematicity is not discounted even for chalcogenides. Another is how does nematicity and nematic fluctuations interact with superconductivity. Again, the pnictides and chalcogenides differ; the pnictides have superconductivity peaked where the nematic phase ends, but in some chalcogenides, T_c peaks well into the nematic state.

3.3 Superconductivity

Superconductivity is the phenomenon when the resistivity of a material falls exactly to zero below a critical temperature T_c and the magnetic flux is expelled perfectly within the bulk of the material. It was discovered in elemental mercury by H. Kamerlingh Onnes in 1911

[50]. A microscopic theory for superconductivity involving the pairing of opposite spin electrons being mediated by phonons was developed by Bardeen, Cooper, and Schrieffer (BCS) by 1957 [3]. Some experimental facts that led to the development of this theory include the opening of a gap in the electronic density of states, which pointed to the electrons forming pairs, and the isotope effect which hinted at the involvement of a phonon. BCS theory predicts several trends: (i) BCS superconductors are good metals in their normal state (ii) BCS superconductors obey the same relation between the size of the gap and T_c: $2\Delta(T = 0) = 1.76 k_B T_c$ (iii) the presence of magnetism or magnetic impurities hinders superconductivity (iv) heat capacity is suppressed at low temperatures. The BCS explanation of superconductivity worked well for elemental and other early superconductors until the discovery of heavy fermion superconductors in 1979 [7, 51]. These materials have electron effective masses much larger than the free electron mass and large C/T ($T \to 0$) and large magnetic fluctuations, all making a BCS explanation unlikely.

The field of unconventional superconductors really exploded in 1986 with the discover of high-temperature superconductivity in the cuprates [4]. Some common characteristics of unconventional superconductors include: (1) the breaking of an additional symmetry at T_c, (2) proximity to other exotic broken-symmetry states (the normal state is a non-Fermi liquid), (3) the presence of strong electron correlations. While different classes of unconventional superconductors exhibit myriads of exotic phenomena, one unifying theme is that their Cooper pairing cannot be explained with electron-phonon coupling of BCS theory [31]. An overarching question in studying unconventional superconductors is, "What are the pairing symmetries and pairing mechanisms?". Stated more plainly: "Which electrons are involved in forming Cooper pairs?" and "What interaction(s) are helping the electrons form the pairs?".

In BCS superconductors, the size of the gap is symmetric in $\mathbf{k}$-space. Figure 3.4a shows a schematic of a gap function $\Delta(\mathbf{k})$ for an s-wave superconductor, which has spherical symmetry like the s-orbitals for the hydrogen atom. However, for unconventional superconductors

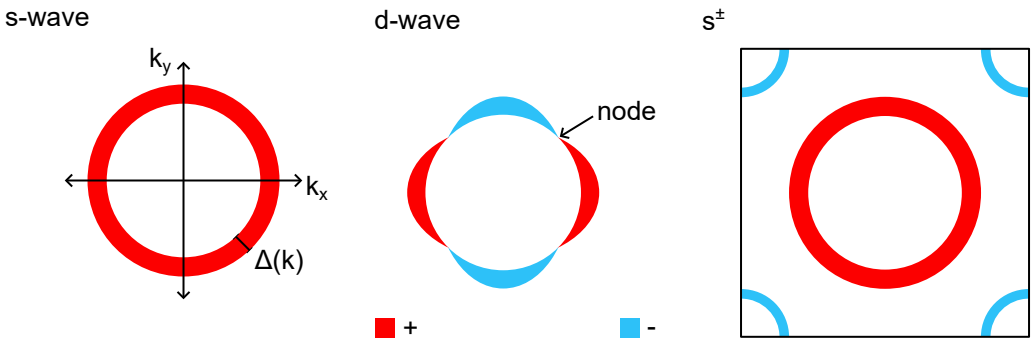

Figure 3.4: Schematic drawing of superconducting gap symmetries.

the size of the gap can depend on the momentum of the electrons involved. In fact, the size of the gap can be zero for some momenta, meaning there are nodes in the superconducting gap structure. One unconventional superconducting gap structure is d-wave (Fig. 3.4b), which has nodes and a the order parameter has a different sign for the x and y directions [52]. Another is $s^{\pm}$, which specifically requires more than one band and has a different order parameter sign for hole and electron bands (Fig. 3.4)c. While the simplest conception of the $s^{\pm}$ scenario has the gap structure isotropic within in each band, this is not necessarily the case; anisotropy and accidental nodes can occur. The d-wave and $s^{\pm}$, are commonly discussed pairing symmetries because d-wave is pretty well established to occur in cuprate superconductors and $s^{\pm}$ has been a hopeful candidate in the Fe-based superconductors [53]. However more exotic and complicated order parameters have been discussed and might be necessary to reconcile all experimental phenomena.

In the iron-based superconductors, likely proponents for pairing mechanisms are spin fluctuations and nematic fluctuations. In $FeSe_{1-x}S_x$ Se-77 NMR shows that spin fluctuations peak near the maximal T_c at $x = 0.9$ [54], while elasto-resistance measurements show nematic fluctuations are strongest near the nematic phase transition ($x = 0.18$) [20]. An interpretation of these experiments is that spin fluctuations are responsible for the formation of Cooper pairs in $FeSe_{1-x}S_x$. However, other experiments show an abrupt change in the superconducting state across the nematic transition near x = 0.17 [55]. For example, STS

experiments have shown that the superconducting gap suddenly shrinks when x is increased above x_c [23]. Those authors interpreted this observation as there being two distinct pairing mechanisms in the two phases, and particularly point to an orbitally-selective paring scenario like the one discussed in [56]. The superconducting gap in pure FeSe is highly anisotropic, but whether it has nodes is still up for debate.

There is some experimental evidence that the pairing strength in $FeSe_{1-x}S_x$ is also exotic. Most superconductors, even unconventional ones, exist in the weak coupling (BCS) regime. In this regime the pairing energy is much smaller than the Fermi energy ($\Delta << \epsilon_f$) and the pair distance is large compared to the average electron distance. In this case when the pairs form they also condense at nearly the same temperature. Cooper pairs that form in the strong coupling limit are within the Bose-Einstein condensate (BEC) regime. Here the strong coupling causes the pairs to be tightly bound, so the spacing between them is small compared to the average electron distance. Since the pairing interaction is so strong, pairs form at temperatures well before they are able to condense. Cooper pairs in $FeSe_{1-x}S_x$ might have an intermediate coupling strength, known as the BCS-BEC crossover regime. Measurements of the superconducting gap using STS put the ratio of the gap to Fermi level to be at least 0.1, which would put it in the crossover regime [32]. However, direct experimental evidence of preformed pairs is lacking.

3.4 Charge Order

Even though I am going to use the term charge order, understanding the picture for a conventional charge density wave (CDW) is important. CDW are often understood with the picture of the Peirels distortion, which occurs when there is a Fermi surface instability. The instability occurs when lowering the energy of the electrons near the Fermi level and opening a gap costs less energy than distorting the ions in the lattice [57]. When the lattice is spaced uniformly, the the electron density is also uniform. After the lattice distorts, there will also a

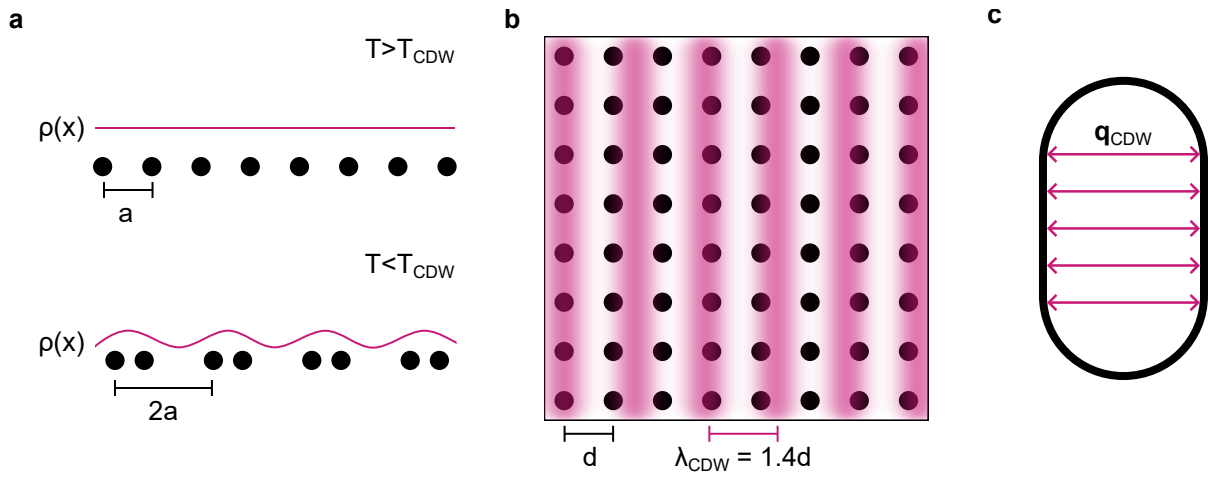

Figure 3.5: **a** Schematic drawing of the lattice and charge density $\rho(x)$ for a Peirels distortion. **b** Schematic drawing of an incommensurate CDW with C_2 symmetry and wavelength of 1.4 lattice constants. **c** A schematic example of a partially nested 2D Fermi surface. The three panels are independent schematics.

be modulation of the electron density, which will have a characteristic wavelength λ_{CDW} (Fig. 3.5a). The periodicity of the modulation can either be an integer multiple (commensurate) of the periodicity of the lattice, or a non-integer multiple (incommensurate). The Fermi surface of a one-dimensional metal at low temperatures will always be unstable. In higher dimensions, a highly nested Fermi surface can also cause the instability. A Fermi surface is nested if single wavevector connects multiple points on the Fermi surface (see Fig. 3.5b). However, this mechanism is too simplistic to account for most real CDW systems [58]. Many CDW systems do not have nested Fermi surfaces and having a nested Fermi surface does not necessarily mean CDW will occur. Some additional interaction, such as electron-phonon coupling, is needed to explain the formation of most CDW, and myriads of interactions can drive CDW.

To allow for the broadest possible manifestations and mechanism, I will stick to the term charge order. Charge order is an electronic state which in which the electrons reorganize into a periodic modulation that breaks the translational symmetry of the lattice. Sometimes the terms charge order and charge density wave (CDW) are used interchangeably and other times ascribe different definitions to the two terms. For example, charge order can be

broadened to include $\mathbf{q} = 0$ orders such as nematicity, while CDW are strictly $\mathbf{q} \neq 0$ orders. Further complicating the vocabulary is the word "stripes", which refers to a translational and rotational symmetry breaking order, i.e. a charge order which has C_2 symmetry instead of C_4. Sometimes stripes is generalized to include both charge and spin order [26]. In this work I will reserve charge order to refer to finite $\mathbf{q}$ modulations in the charge channel, and stripes will simply mean charge order with C_2 symmetry. The concept of charge order will be most important for Chapter 5, which is studying charge order in the cuprates, but will be discussed in Chapter 4 as well.

Chapter 4

Electronic States of Tetragonal Fe(Se,S)

The measurements presented in this chapter were done with the help of many others. Helping with the STM/S measurements were Kirsty Scott, Timothy Boyle, Adrian Gozar and Zeke Zhao. The ARPES measurements took place at the QMSC beamline at the Canadian Lightsource with the help of beamline scientists Sergey Gorovikov and Tor Pedersen. Much assistance was given by Sergey Zhadanovich, Matteo Michiardi and Ryan Day from the group of Prof. Andrea Damascelli. The theoretical calculations were performed by Stefan Botzel from Ilya Eremin's group. The samples were grown by Journey Byland in Valentin Taufour's group. The results are published in npj Quantum Materials 8:60 (2023) [59].

4.1 Introduction

The $FeSe_{1-x}S_x$ system is unusual for an iron-based superconductor because it has no long-range magnetism at ambient pressure. Its superconducting T_c also peaks well inside of the nematic state, whereas for most iron-based superconductors this peak occurs where the nematic state ends. The parent compound has been intensely investigated, and there have been a few general studies for many sulfur concentrations, measurements focused solely within the tetragonal state are lacking. Scanning tunneling microscopy/spectroscopy (STM/S) can access a lot of information on the system because it can measure both occupied and unoccupied states, has high energy resolution, and is spatially resolved. We performed STM/S studies on $FeSe_{0.81}S_{0.19}$ to obtain detailed measurements of the electronic band structure. Using a new spatially-resolved analysis which separates the images into regions near and away from the iron-vacancy defects, we find that the two regions contain different scattering features. In

collaboration with Professor Ilya Eremin's group at Ruhr University Bochum, we calculated the local density of states calibrated by ARPES measurements to compare with our STS measured band structure. This comparison shows good agreement and reveals that some scattering features come from parts of the Brillouin zone not previously resolved by STS measurements. However, there is one intense feature just above the Fermi level centered at $\mathbf{q} = 0.12$ Å^{-1} that remains unaccounted for. Closer examination of this feature reveals that it is non-dispersive for a range of 10 meV. We also performed a local rotational symmetry analysis and found that the electronic stripes are comprised of domains with 2-fold symmetry and we found that the boundaries are located near iron-vacancies. Finally we compare the phenomenology of the electronic stripes in $FeSe_{1-x}S_x$ to the well known charge order in cuprate superconductors, such as $Bi_2Sr_2CaCu_2O_{8+x}$.

4.2 Methods

Single crystals of FeSe and $FeSe_{1-x}S_x$ were grown using the chemical vapor transport method in a tilted furnace following the methods outlined in [60]. Pure samples were characterized using a powder x-ray diffractometer. To determine the relationship between actual and nominal sulfur substitution levels, samples were characterized using a scanning electron microscope equipped with an energy dispersive x-ray (EDX) spectroscopy probe and counting S atoms in STM topographies. Several platelets with dimensions between 1-2 mm by 1-2 mm were selected from each batch for characterization.

STM/S measurements were done with a customized Unisoku USM-1300 instrument. The samples were cleaved *in situ* in an ultra-high vacuum environment with pressures below 10^{-9} Torr. All STM/S measurements were performed at 4.2 K. Differential conductance measurements (dI/dV) were performed using a lock-in technique. Tunneling current and bias setpoint conditions, as well as lock-in parameters, are summarized in Table 4.1. All Fourier transformations shown in this work were performed using a discrete fast Fourier

transform algorithm on a normalized dI/dV map, unless stated otherwise.

Table 4.1: Parameters of STM measurements on $FeSe_{1-x}S_x$.

x	Bias (mV)	Current (pA)	Scan size (nm^2)	Grid size	Modulation amplitude (mV)
0	-20	500	10x10	256x256	N/A
0.19	-10	1500	80x80	1024x1024	N/A
0	-42	200	170x170	256x256	1
0	-20	200	20x20	32x32	0.25
0.19	-50	450	170x170	256x256	0.75
0.19	-50	450	46x46	256x256	0.75
0.19	-60	450	46x46	256x256	0.75
0.23	-42	250	170x170	256x256	1.5

ARPES measurements were carried out on the Quantum Materials Spectroscopy Centre beamline at the Canadian Light Source, with vertically and horizontally polarized light with photon energy ranging from 18 to 40 eV (see figure captions). Samples were cleaved *in situ* and measured at pressure lower than 5×10^{-11} Torr and a temperature of 9 K. The combined beamline-analyzer (Scienta R4000) resolutions in angle and energy are better than 0.1° and 9 meV, respectively, for the combinations of beamline parameters (monochromator grating, exit slit, temperature, photon energy) used.

The samples were oriented using the well known shapes of the Fermi surface. In pure FeSe, only the pockets at the Γ point are needed to determine the orientation, but in the tetragonal samples the Γ pockets are isotropic. Instead, finding the M point was necessary to know the orientation. Once the orientation was determined the desired features were centered in the detector. As the beamline was still in the commissioning phase, some operations were not fully automated and difficult to perform online. Changing the photon energy was one of these manual operations, so a full energy dependence of the pockets at the Brillouin zone center was not measured. Instead we relied on the photon energy values reported in the literature for similar S concentrations [49]. A gold wire calibration to determine the Fermi level was unavailable, so the Fermi level was found by fitting an EDC to a temperature broadened Fermi-Dirac function in a region where no band was crossing.

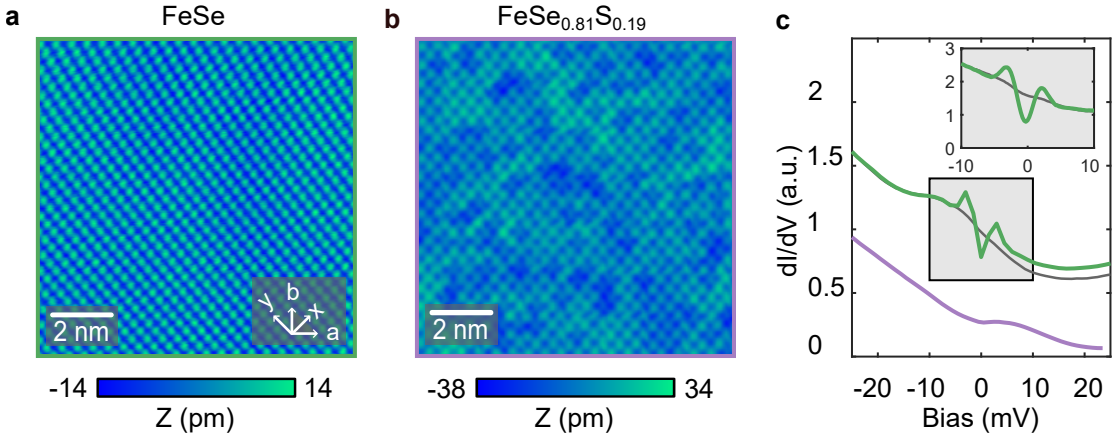

Figure 4.1: **a**, **b** Representative constant current topographic images of FeSe and $FeSe_{0.81}S_{0.19}$ showing the atomically resolved (Se,S) termination layer. **c** Representative spatially averaged differential conductance (dI/dV) spectra of FeSe (green) and $FeSe_{0.81}S_{0.19}$ (purple). The grey curve is the spectrum of $FeSe_{0.98}S_{0.02}$ with a 10 T magnetic field applied normal to the a-b plane to suppress superconductivity. The inset shows two spectra with higher energy resolution in the range of the superconducting gap, taken on a pure FeSe sample with no field applied (green) and with 10 T (grey).

4.3 STM/S Results

Overview of Results

While the primary focus of this work is on tetragonal samples with x = 0.19, we also show results on pure FeSe to compare the two. The topography in Fig. 4.1a shows the atomic resolution of a clean selenium termination layer of pure FeSe. In the 19 % sulfur sample, the topography (Fig. 4.1b) shows cross-like defects which are due to sulfur atoms replacing selenium, which appear to be uniformly distributed. Fig. 4.1c shows spatially averaged differential conductance (dI/dV) spectra of the two sulfur concentrations showing the superconducting gap in the pure FeSe case. The system is not fully gapped, and the gap has particle-hole asymmetry, which is explained by strong electronic correlations. For 19% sulfur, T_c is only slightly above the measurement temperature of 4.2 K, so the superconducting gap is not resolved.

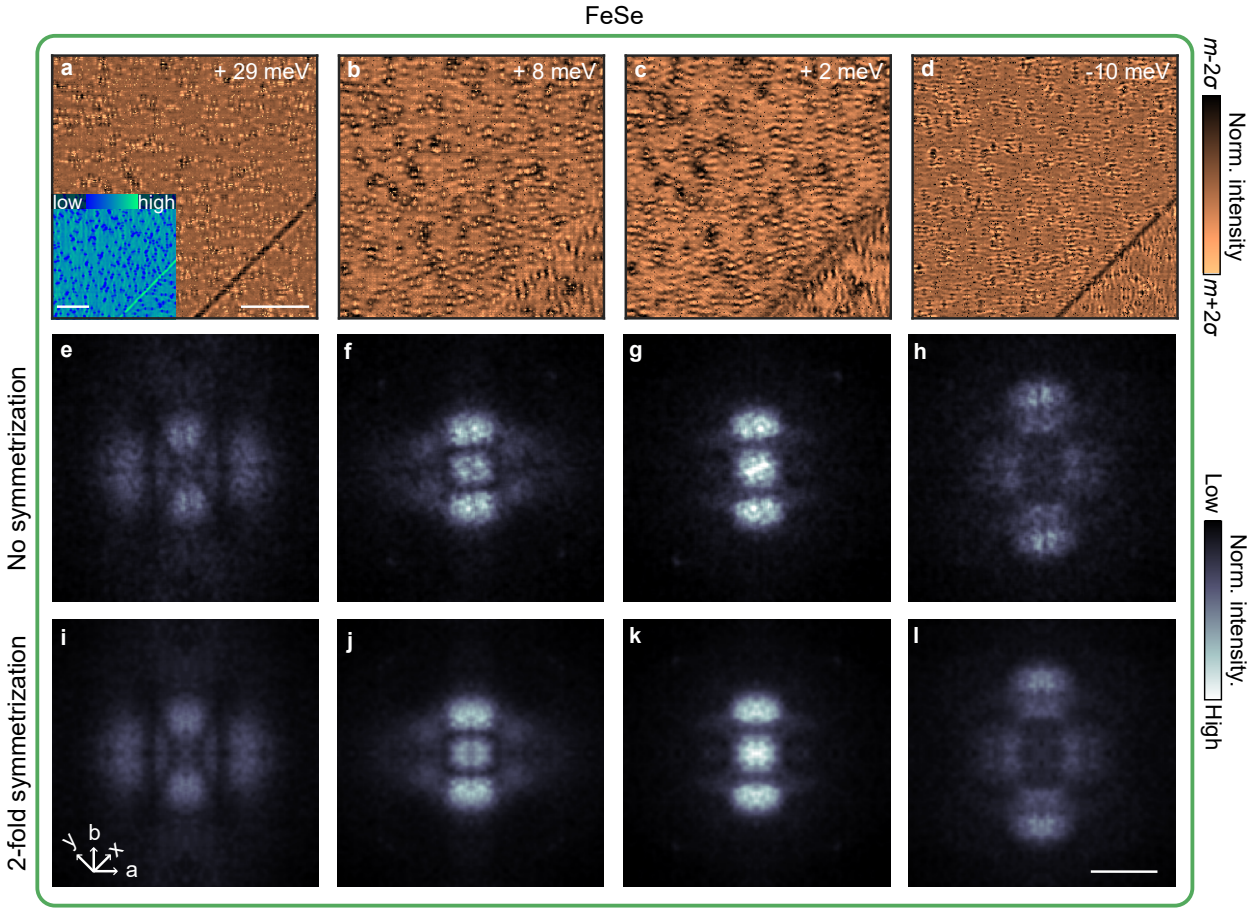

Figure 4.2: **a-d**,**i-l** dI/dV maps on FeSe at selected energies. The maps were normalized by their standard deviation after subtracting the mean. **e-h**,**m-p** Fourier transform of the real-space images.

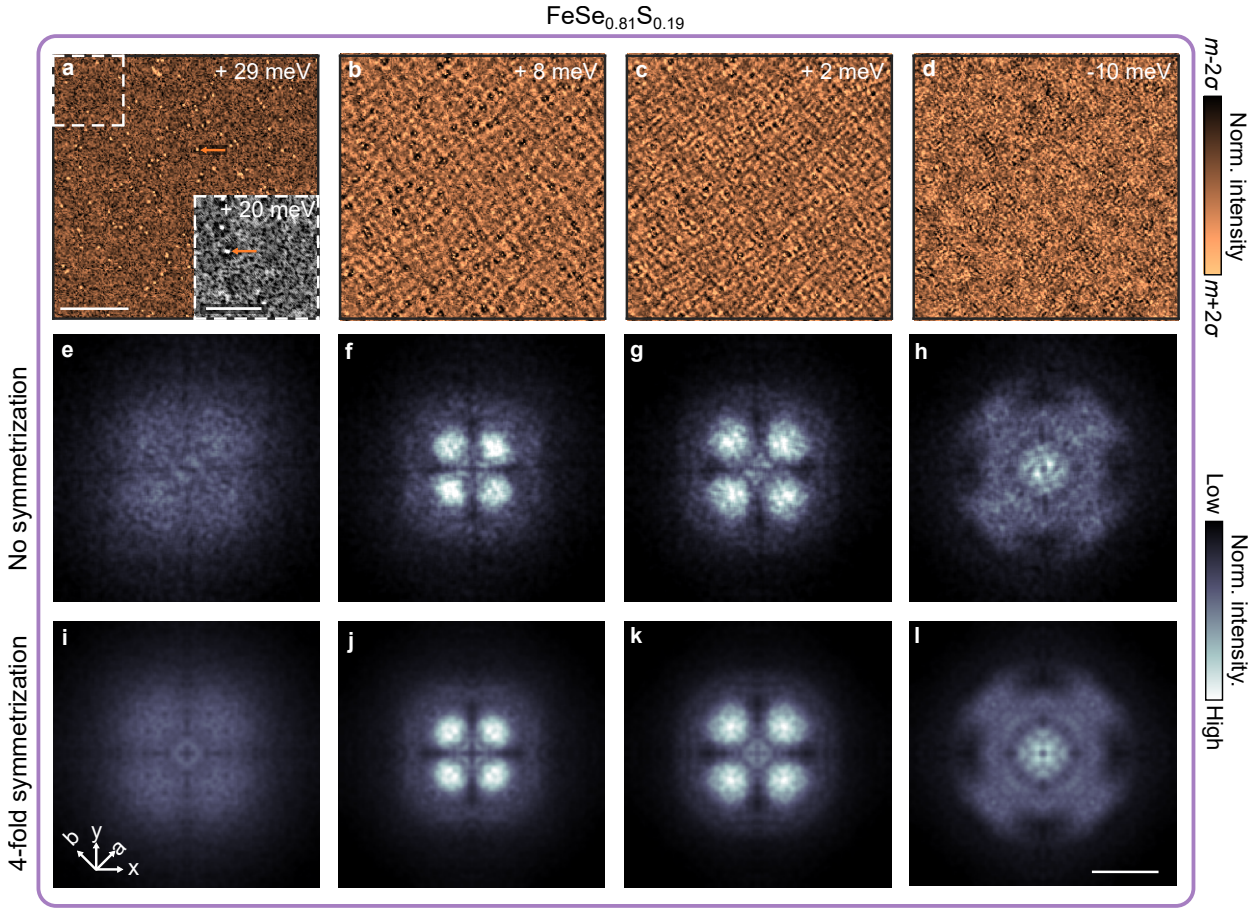

Figure 4.3: **a-d**,**i-l** dI/dV maps on $FeSe_{0.81}S_{0.19}$, at selected energies. The maps were normalized by their standard deviation after subtracting the mean. **e-h**,**m-p** Fourier transform of the real-space images.

The spectroscopic maps on FeSe (Fig. 4.2 a-d) show the local density of states, including many iron vacancies acting as the scattering centers for quasiparticle interference (QPI), which is reflective of the electronic band structure. The Fourier transforms (Fig. 4.2 e-f) show several peaks which have two-fold symmetry. There is also a nematic domain boundary in the bottom right. The dI/dV patterns on either side of the domain boundary are rotated 90° from one another. Both of these observations are expected in the nematic state. The dI/dV patterns change in wavelength as a function of energy, which is indicative of their QPI origins.

In the spectroscopic maps for x = 0.19, dI/dV patterns are four-fold symmetric and iron-vacancies are harder to distinguish. For the energy cut at +29 meV, no QPI patterns can easily be seen in the real-space, which can be confirmed by the lack of coherent QPI peaks in the Fourier transform. However, iron-vacancies appear as bright spots above an inhomogeneous background, which will be important for scatterer-resolved QPI analysis in a later section. In the energies just above the Fermi level, there is a checkerboard-like pattern in the real-space images that shows up as well-defined point-like peaks at $q_{a,b} \approx 0.12$ Å^{-1} in the Fourier transform. Below the Fermi level, smaller wavelength patterns appear and in the Fourier transforms there are peaks along q_x and q_y of similar intensity to those along q_a and q_b.

To track the energy-momentum structure of peaks in the Fourier transform we took line cuts along the directions of interest and stack them in energy. For pure FeSe, the q_a and q_b directions are inequivalent, so their line cuts are taken separately. Since $FeSe_{0.81}S_{0.19}$ has four-fold symmetry, cuts are taken along $q_{a=b}$ and $q_{x=y}$. Fig. 4.4a,b shows the energy-momentum structure for pure FeSe along the two inequivalent Fe-Fe bond directions marked in Fig. 4.2. The stark differences between to the two images indicate strong in-plane anisotropy, which is consistent with the nematic band structure. In the q_b direction we identify four features with hole-like dispersion, which is in agreement with ref. [23]. In the tetragonal x = 0.19 samples, since the q_a and q_b are equivalent, cuts are instead taken along both the Fe-Fe bond

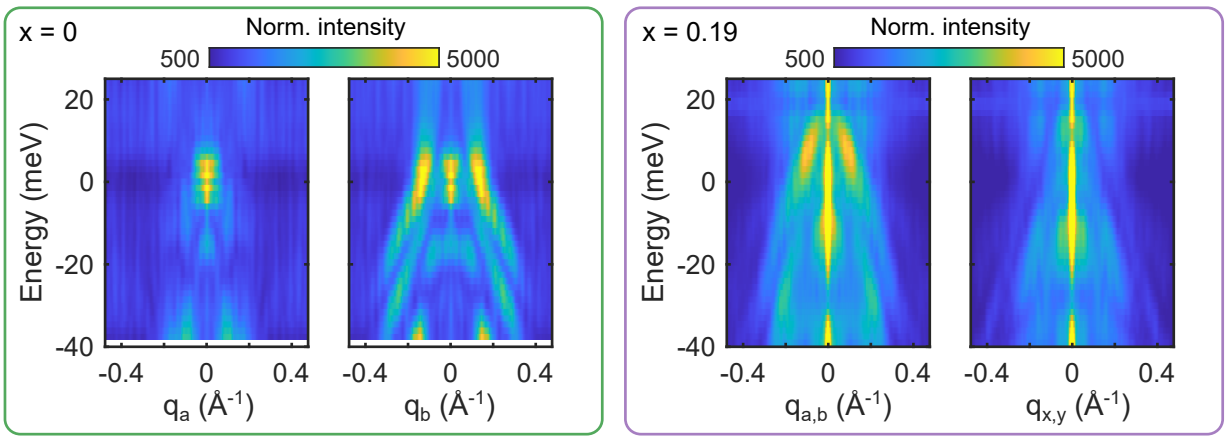

Figure 4.4: **a**,**b** Energy momentum structure of the dI/dV maps on pure Fese in Fig. 4.2a-d with cuts taken along the $q_b = 0$ (a) and $q_a = 0$ (b) high-symmetry directions. **c**,**d** Energy momentum structure of the dI/dV maps on $FeSe_{0.81}S_{0.19}$ in Fig. 4.2a-d with cuts taken along the Fe-Fe bond direction (a) and the Se-Se bond direction (b).

direction and the Se-Se bond directions. At least two hole-like features are distinguishable in the Fe-Fe direction, and possibly three are resolved in the Se-Se direction. Direct comparison with ARPES and theory can help to explain the missing QPI bands, which we will show in a later section, but first we will utilize a new spatial analysis of STS data.

Scatterer-Resolved Quasiparticle Interference

It is possible that the random distribution sulfur is acting as an additional scattering potential or just generally broadening the QPI signals. We can use the spatial resolution of the STM to test this by separating iron-vacancies from the rest of the image. If the random distribution of sulfur is acting as an additional scattering potential, it might be the case that some scattering vectors couple more to one impurity potential over the other. Or, in the case that the sulfur is broadening the QPI signal, maybe this effect will be lessened if we restrict the analysis to be near the iron-vacancies where the QPI is the strongest. We took similar measurements to those in Fig. 4.4b,c over a smaller field of view with just a few iron vacancies present so we can easily separate the image into regions near and away from iron-vacancies. This was done using a simple algorithm so that we can scale the procedure to larger images.

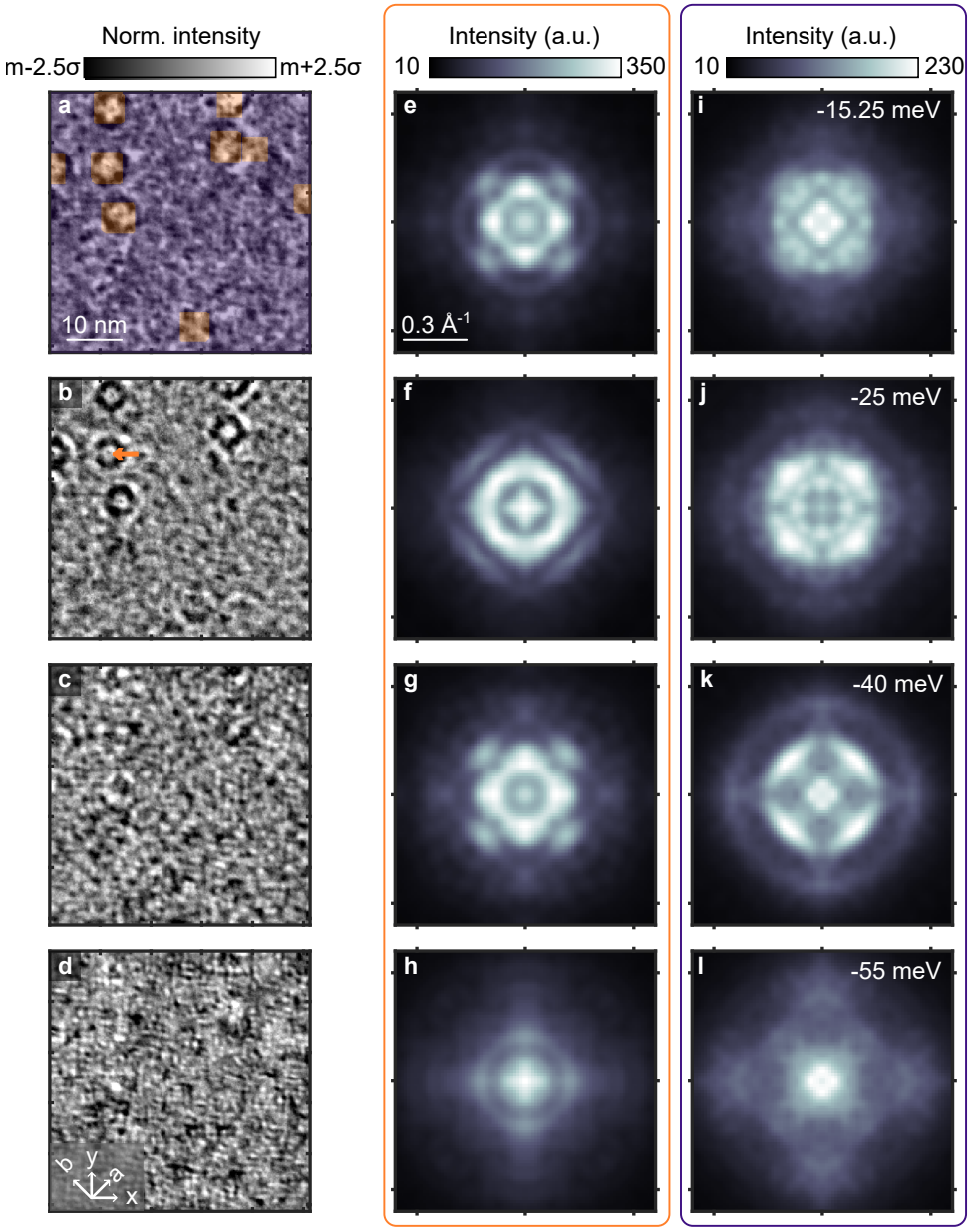

Figure 4.5: **a-d** dI/dV maps on $FeSe_{0.81}S_{0.19}$, at selected energies. **e-h** Fourier transform of the near-iron vacancy region (orange) of the real-space images in **a-d**. **j-m** Fourier transform of the off iron vacancy region (blue) of the real-space images in **a-d**. The dI/dV maps in a-d were normalized, where m is the map mean and σ is the standard deviation.

To select the regions of iron-vacancies, we used an energy cut at + 20 meV or higher where the iron-vacancies appear as bright spots and there is little other QPI present. We then select the pixels that are above a threshold of 3.2 standard deviations above the mean of the image.

Fig. 4.5a-d show the real-space spectroscopic map over selected energy ranges of a 45 nm x 45 nm region including 8 iron-vacancies. The QPI patterns near the iron vacancies appears as a C_4 symmetric flower-like pattern that gets smaller with decreasing energy. At very low energies the flower pattern disappears and the image is dominated by a smaller wavelength feature in the Se-Se bond direction. Away from the iron-vacancies, patterns with a much smaller wavelength are visible. We separated the map into regions near (orange) and away (blue) from iron-vacancies using the algorithm described above and took the Fourier transforms of the two regions separately. There are notable differences in the Fourier transforms from the two regions. The peaks coming from the orange region are typically sharper and more distinct. Also, for a given energy, different peaks are more prominent in the different regions. Also note that for both regions, the peaks in the Se-Se bond directions are comparable in intensity and sharpness to those in the Fe-Fe direction, which is unusual. The utility of the scatterer-resolved QPI method can be further demonstrated by looking at the energy-momentum structure of the two regions.

Fig. 4.6 shows the energy-momentum structure in the Se-Se direction for a small energy range below the Fermi level for the spatially averaged full map (a) and the orange (b) and blue (c) regions separately. In Fig. 4.4a, there is a broad, dispersive band in the -30 to -10 meV range. But for the same energy range in the blue region, two separate sharp bands which are marked by white lines can be distinguished. In the orange region, the black line marks a single band in this energy range. By overlaying these lines from the orange and blue regions onto the image from the full map, one can identify the broad band to be coming from the three overlapping bands. It appears that the large quantities of sulfur are promoting QPI and the scatter-resolved QPI method is a useful tool to better resolve the electronic

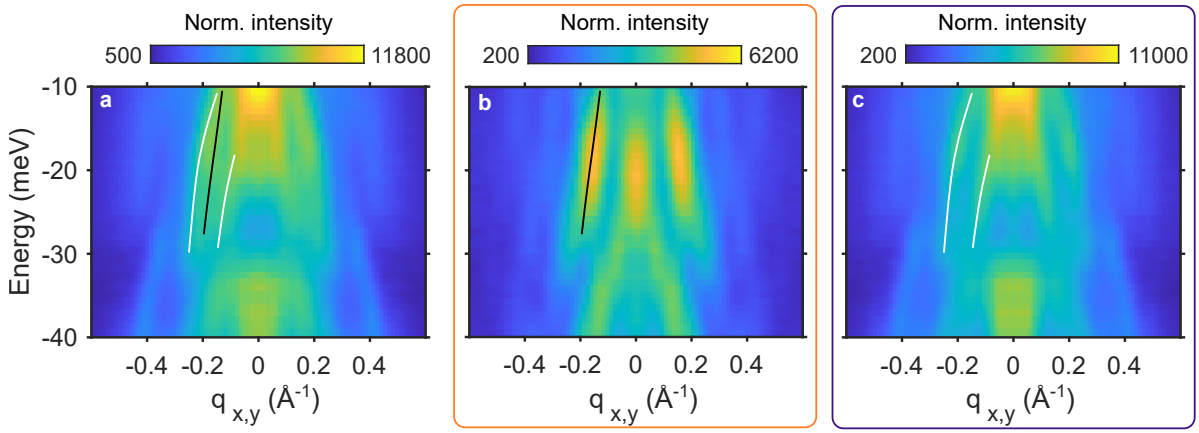

Figure 4.6: Dispersion maps along Se-Se bond direction taken over the full map (**a**), the orange region (**b**) and the blue region (**c**) of Fig. 4.2a. Lines drawn on b and c are guides to the eye highlighting bands in that region, and these same lines are shown in a.

states in samples with high disorder.

4.4 ARPES Results

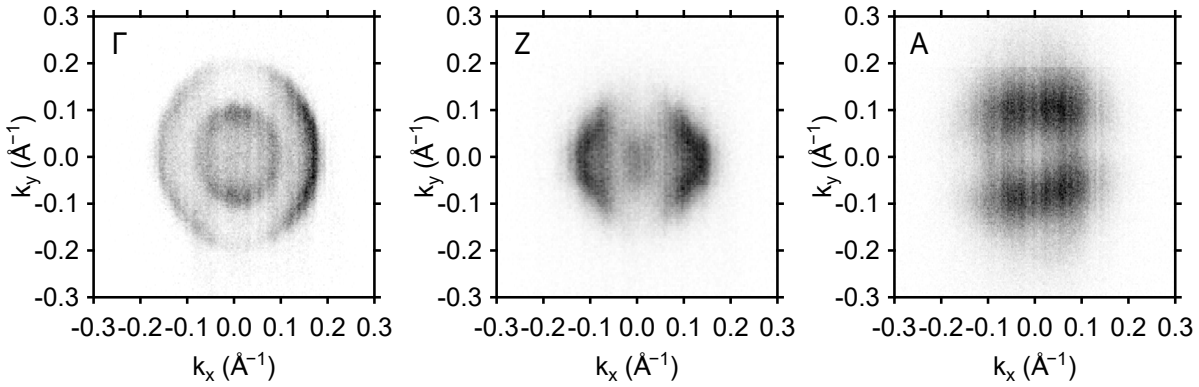

Figure 4.7: **a-c** Left side: ARPES constant energy contours at the Fermi level near the Γ, Z, A points of $FeSe_{0.77}S_{0.23}$ taken with vertically polarized light with photon energies $PE = 38\,\text{eV}$, $PE = 19\,\text{eV}$, and $PE = 18\,\text{eV}$, respectively.

Fig. 4.7 shows the Fermi surface of $FeSe_{0.77}S_{0.23}$ at the Γ (a), Z (b), and A (c) points of the Brillouin zone. At the Γ point, there are two concentric pockets, the inner-most being nearly the top of the band. Matrix element effects make resolving the top/bottom of the

outer pocket difficult, so it could be either a rotated square or an oval. At the Z point, the pockets are larger due to the 3D nature of these pockets, and the despite the matrix element effects, both pockets can be resolved. High statistics cuts were taken along the $\mathbf{k}_y$=0 direction for all points and are shown in Fig. 4.8. These show that the pockets at Γ and Z are hole-like, while the pocket at the A point is electron-like. The positions of the bands were determined by fitting the MDCs to an appropriate number of Lorentzian peaks and a small background. In regions near the top of bands fits to the EDCs were used instead.

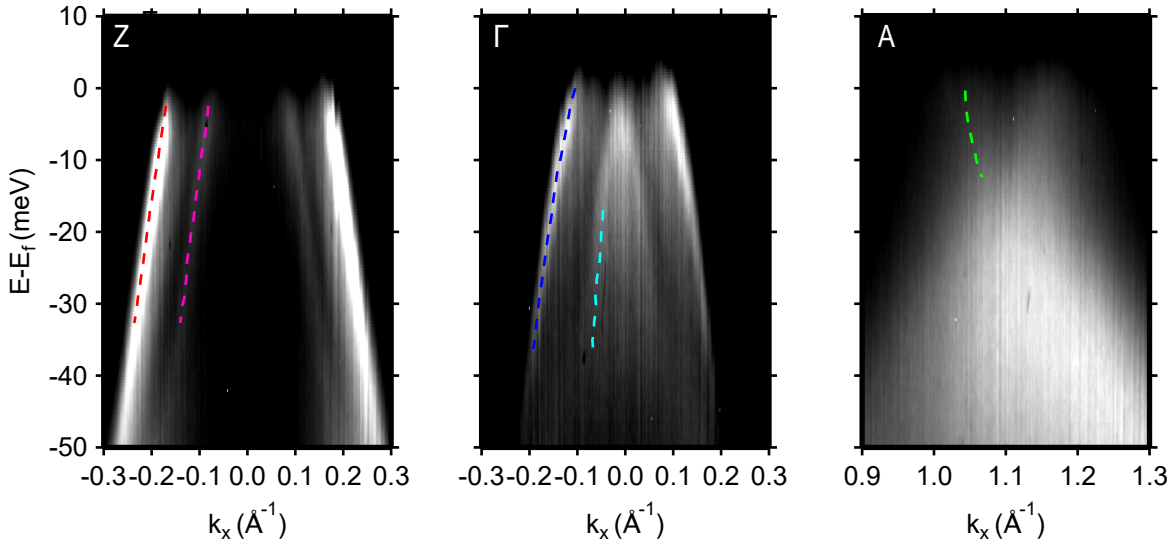

Figure 4.8: **a-c** Left side: ARPES images near the Γ, Z, A points of $FeSe_{0.77}S_{0.23}$ taken with vertically polarized light with photon energies $PE = 38\,\text{eV}$, $PE = 19\,\text{eV}$, and $PE = 18\,\text{eV}$, respectively. The lines on the left are determined by fitting the momentum distribution curves (MDCs) to Lorentzian peaks.

4.5 Theoretical Model

We present our theoretical model used to calculate QPI patterns to compare with measurements from STS. The calculations were initially done by Ilya Eremin's group, but later expanded by Dr. Adrian Gozar. I checked and used the code that Adrian wrote to perform the calculations and produce all of the figures. Briefly, some important assumptions we made are: i) 2D electron pockets at the Brillouin zone corners, ii) no spin-orbit coupling at the

Brillouin zone corners, iii) isotropic Fermi surface at the zone center, iv) small $\mathbf{q}$ interband scattering is allowed.

In the normal state of $FeSe_{0.77}S_{0.23}$, the electronic Hamiltonian near the Γ- $(0,0,0)$ and Z-points $(0,0,\pi)$ reads [61, 46]

$$H_{\Gamma/Z} = \sum_{\mathbf{k}} \Psi^{\dagger}_{\Gamma/Z}(\mathbf{k}) \left[h^{0}_{\Gamma/Z}(\mathbf{k}) + h^{\mathrm{SOC}}_{\Gamma/Z}(\mathbf{k}) \right] \Psi_{\Gamma/Z}(\mathbf{k}), \tag{4.1}$$

where $\Psi_{\Gamma/Z} = (d_{yz,\uparrow}, d_{xz,\uparrow}, d_{yz,\downarrow}, d_{xz,\downarrow})^{T}$ is the four component spinor with the momentum label $(\mathbf{k})$ being implicit and measured as deviation from the Γ- or Z-point. The term

$$h^{0}_{\Gamma/Z}(\mathbf{k}) = \begin{pmatrix} \epsilon_h - \frac{k^2}{2m} - \frac{b}{2}(k_x^2 - k_y^2) & -2ck_xk_y \\ -2ck_xk_y & \epsilon_h - \frac{k^2}{2m} + \frac{b}{2}(k_x^2 - k_y^2) \end{pmatrix} \otimes \sigma_0 \tag{4.2}$$

models the electronic dispersion while the effect of spin-orbit coupling is captured by

$$h^{\mathrm{SOC}}_{\Gamma/Z}(\mathbf{k}) = \frac{\lambda_{\mathrm{SOC}}}{2} \tau_2 \otimes \sigma_3. \tag{4.3}$$

Here Pauli matrices σ_i and τ_i act on the spin and orbital space, respectively. The fitting parameters for the electronic states near the Γ and Z points, which enter into Eq. 4.2, are listed in Table 4.2. The resulting band dispersion in direct comparison with our ARPES data is shown in Fig. 4.9a,b for the Γ-point and in Fig. 4.9c,d for the Z-point.

For the electron pockets near the X and Y points of the one-iron Brillouin zone which are folded to the A-point in the two-iron unit cell, the Hamiltonian has the form [61, 46]

$$H_A = \sum_{\mathbf{k}} \left(\Psi^{\dagger}_{Y}(\mathbf{k}), \Psi^{\dagger}_{X}(\mathbf{k}) \right) \begin{pmatrix} h_Y(\mathbf{k}) & 0 \\ 0 & h_X(\mathbf{k}) \end{pmatrix} \begin{pmatrix} \Psi_Y(\mathbf{k}) \\ \Psi_X(\mathbf{k}) \end{pmatrix}. \tag{4.4}$$

The spinors are $\Psi_Y = \left(d_{xz,\uparrow}, d_{xy^Y,\uparrow}, d_{xz,\downarrow}, d_{xy^Y,\downarrow}\right)^{T}$ and $\Psi_X = \left(d_{yz,\uparrow}, d_{xy^X,\uparrow}, d_{yz,\downarrow}, d_{xy^X,\downarrow}\right)^{T}$, where again the $(\mathbf{k})$ dependence is implicit and considered as deviation from the (π,π,π) A-point.

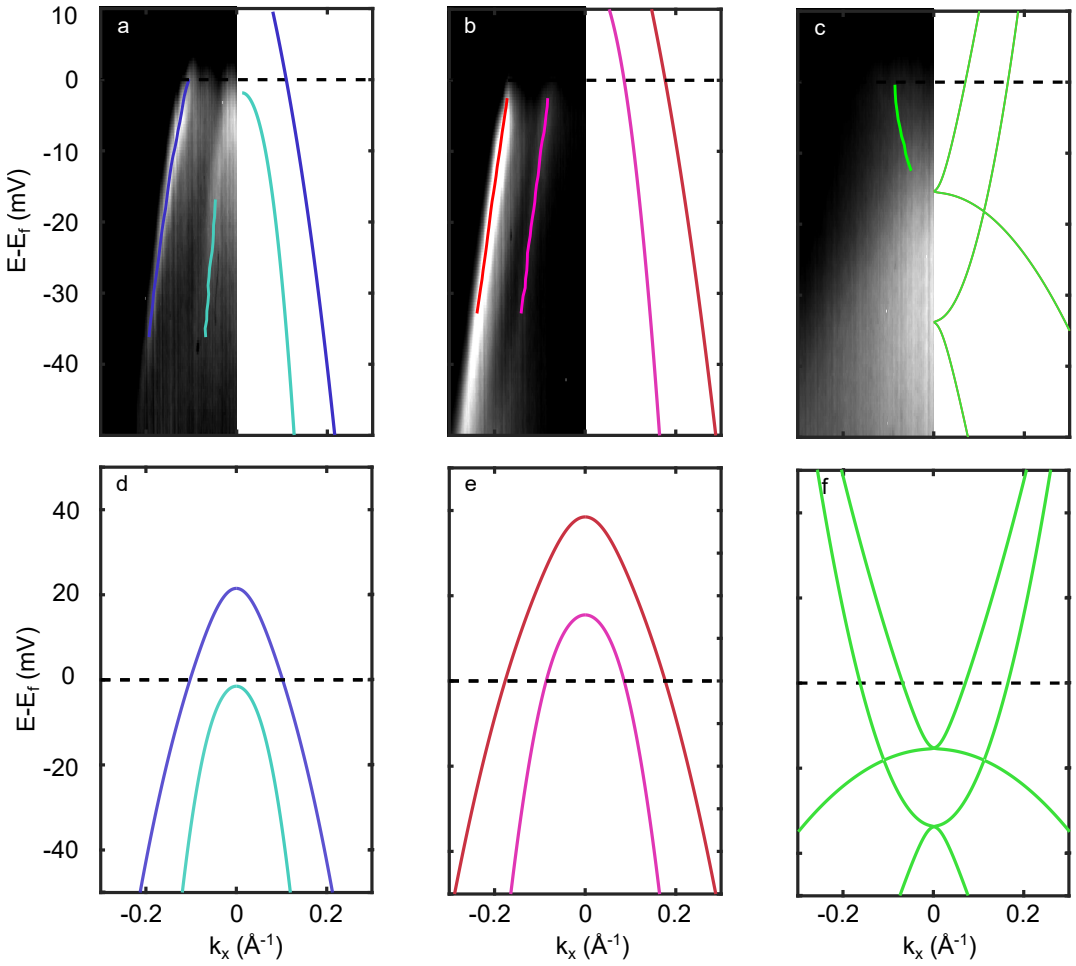

Figure 4.9: **a-c** Left side: ARPES image near the Γ, Z, A points of $FeSe_{0.77}S_{0.23}$. The lines on the left are determined by fitting the momentum distribution curves (MDCs) to Lorentzian peaks. Right side: modeled band structure adjusted to best match the bands measured by ARPES. textbfd-f Same calculations shown over the full k_x range and a broader energy range. ARPES measurements at the Γ, Z, and A were taken with photon energies $PE = 38\,\text{eV}$, $PE = 19\,\text{eV}$, and $PE = 18\,\text{eV}$, respectively.

Here the electronic dispersion reads

$$H_{X,Y} = \begin{pmatrix} \epsilon_1 + \frac{k^2}{2m_1} \mp \frac{a_1}{2}(k_x^2 - k_y^2) & -iv_{X,Y}(\mathbf{k}) \\ iv_{X,Y}(\mathbf{k}) & \epsilon_3 + \frac{k^2}{2m_3} \mp \frac{a_3}{2}(k_x^2 - k_y^2) \end{pmatrix} \otimes \sigma_0, \tag{4.5}$$

where $v_X(\mathbf{k}) = \sqrt{2}vk_y + \frac{p_1}{\sqrt{2}}\left({k_y}^3 + 3k_y{k_x}^2\right) - \frac{p_2}{\sqrt{2}}k_y\left({k_x}^2 - {k_y}^2\right)$ and $v_Y(\mathbf{k}) = v_X(k_y, k_x)$.

At this point we neglect the effect of spin-orbit coupling at the A-point, which would

lead to hybridization of X and Y pockets, but is found to be weaker than near the center of the zone [62]. The same is true for the less pronounced three-dimensionality of the Fermi surface pockets at the zone corners[48, 63], so for simplicity we keep the parametrization of the A-point throughout. The fitting parameters for the A-point electronic states that enter into Eq. 4.5 are listed in Tab. 4.3. The resulting band dispersion in comparison with our ARPES data is shown in Fig. 4.9e,f.

Table 4.2: Parameters for the states at the Γ and Z point fitted to match ARPES data of Fig. 4.9a and Fig. 4.9b.

	Γ	Z	
ϵ_h	10	27	meV
$\frac{1}{2m_h}$	2661	1848	meVÅ^2
b	2624	1822	meVÅ^2
c	-1312	-911	meVÅ^2
λ^h_{SOC}	15	15	meV

Table 4.3: Parameters for the states at the A point fitted to match ARPES data of Fig. 4.9c.

	A	
ϵ_1	-3.6	meV
ϵ_3	-25.6	meV
$\frac{1}{2m_1}$	4.6	meVÅ^2
$\frac{1}{2m_3}$	603	meVÅ^2
α_1	441	meVÅ^2
α_3	-1308.4	meVÅ^2
v	-221.2	meVÅ
p_{z_1}	-800.3	meVÅ^3
p_{z_2}	-68.1	meVÅ^3

We calculate the QPI energy-momentum structure of the local density of states in the Born limit given by the convolution of the bare Green's functions dressed by the scattering matrix of a nonmagnetic impurity, $\hat{V}$.

$$\rho(\omega, \mathbf{q}) = -\frac{1}{\pi}\mathrm{Im}\mathrm{Tr}\sum_{\mathbf{k}}\hat{G}_{\mathbf{k}}(\omega) - \frac{1}{\pi}\mathrm{Im}\mathrm{Tr}\sum_{\mathbf{k}}\hat{G}_{\mathbf{k}}(\omega)\hat{V}\hat{G}_{\mathbf{k}+\mathbf{q}}(\omega) \tag{4.6}$$

Here the corresponding bare Green's function in momentum space is given by $\hat{G}_{\mathbf{k}}(\omega) = [(\omega + i\delta) - h(\mathbf{k})]^{-1}$, where

$$h(\mathbf{k}) = \begin{pmatrix} h^0_{\Gamma/Z}(\mathbf{k}) + h^{\mathrm{SOC}}_{\Gamma/Z} & 0 & 0 \\ 0 & h_Y(\mathbf{k}) & 0 \\ 0 & 0 & h_X(\mathbf{k}) \end{pmatrix}, \tag{4.7}$$

and $\hat{V} = \mathbb{I}_{3\times3} \otimes (V_0\tau_0) \otimes \sigma_0$ refers to the intraorbital non-magnetic scattering potential leading to small $\mathbf{q}$ intra- and interband scattering processes between hole and electron states, respectively. We use Eq. 4.6 to calculate the resulting QPI patterns as a function of bias voltage (ω) and momentum ($\mathbf{q}$) shown in Fig. 4.10 for the $k_z = 0$ and $k_z = \pi$ cuts, respectively.

4.6 Further STM/S Analysis

Identifying Scattering Processes in QPI

The energy momentum structure we measure with STS should be indicative of the underlying electronic band structure. Fig. 4.10 shows the calculated local density of states for the Γ (a), Z (b), and M/A (c,d) points in the 2-Fe Brillouin zone. For the M/A points both cuts along the Fe-Fe (c) and the Se-Se (d) bond directions are shown; In our calculations, the pockets at Γ and Z are circular, so only one cut for each point is shown. Fig. 4.10 (e-h) shows the experimental energy-momentum structure for the different spatial regions and the two high-symmetry directions. In the Fe-Fe direction of the orange region, there are 3 sharp and distinct bands of similar quality to measurements on pure FeSe. The colored lines are used to compare the theoretical bands to the experimental bands, with each high-symmetry point having its own color. The outer pocket at the Z point either is very weak or not seen. There are regions where the inner Z and outer Γ bands overlap, making definitive assignment in those regions difficult. However, the largest $\mathbf{q}$ feature in Fig.4.10e,f is best explained by

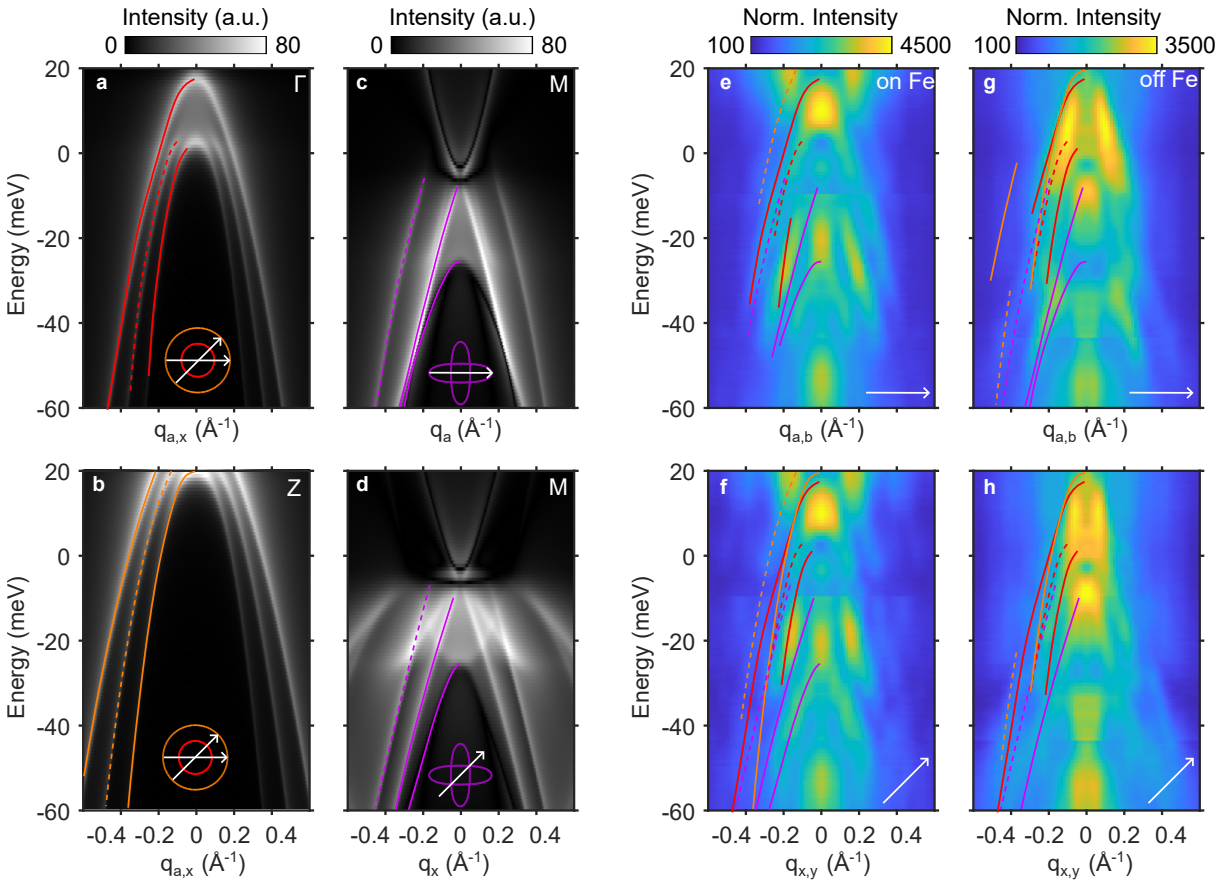

Figure 4.10: **a-d** Calculated dispersion maps of QPI, along the directions indicated in the inset Brillouin zone schematic, obtained from a band structure model fitted to ARPES data. Red, orange, and purple lines are guides to the eye. A dashed line indicates that the feature is due to interband scattering. **e-h** Dispersions maps obtained from the orange region (**e,f**) and the blue region (**g,h**) of Fig. 4.5a

the interband scattering at the Z point (dashed orange line). Also, the smallest **q** features in the experimental data can only be explained by the electron pockets below the Fermi level (purple), which had not been seen before. Finally, there is a region of high intensity just above the Fermi level in the blue region, which does not have good agreement with predicted bands. Next we will look at these features with better energy and momentum space resolution.

Strong Non-Dispersive Signal Above the Fermi Level

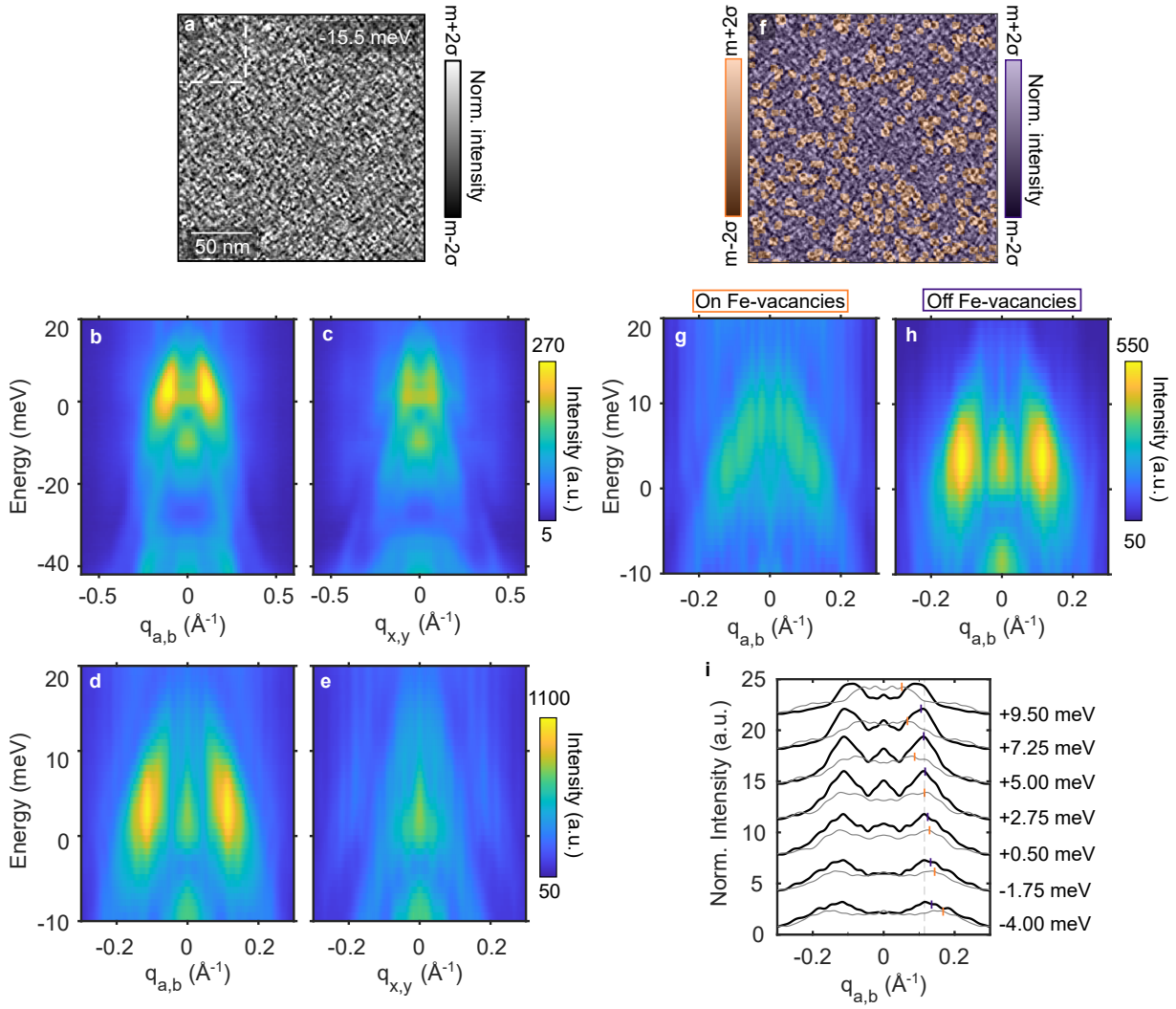

Figure 4.11: **a** dI/dV map on $FeSe_{0.81}S_{0.19}$ at 6 meV. **b**,**c** Dispersion maps along high-symmetry directions obtained from the $45 \times 45\,nm^2$ FOV (see Fig. 4.5). **d**,**e** similar to b,c but obtained from the larger $170 \times 170\,nm^2$ FOV shown in a, and with higher energy resolution. **e** Same as a but with transparent masks separating the map into two regions: near iron vacancies (orange), and away from iron vacancies (blue). **g**,**h** Dispersion maps along the smallest Fe-Fe direction, obtained from the orange and blue regions in f, respectively. **i** Constant energy line cuts of the dispersion maps in h (gray lines) and i (black lines). The orange markers are the locations of the peaks obtained from fits to the linecuts, see SI for more detail.

All previous energy-momentum structures shown have had an energy dependent normalization which is useful for clearly resolving all bands regardless of the scattering intensity

at that energy level. In contrast, Fig. 4.11b,c shows the energy-momentum structure from the full map used in 4.10, but without this energy dependent normalization. This shows that the greatest intensity in dI/dV is concentrated in the Fe-Fe direction between 0 and 10 meV. Next we want to investigate this regions with greatest intensity with better energy and momentum resolution. Fig. 4.11a shows a real-space dI/dV map over a 170 nm x 170 nm field of view which will yield energy-momentum structures with 4.25 times better momentum space resolution than those in Figs.4.10. The energy-momentum structure over the entire field of view (Fig 4.11d,e) shows there is a strong non-dispersive feature, but also a weaker dispersive feature. Referring back to Fig. 4.3b,c, one can actually see this modulation in the real-space, and it appears to pervade the entire image, not just concentrate around iron-vacancies. This can be further tested by using the scatterer-resolved QPI analysis. Fig. 4.11f shows Fig. 4.11a masked into near (orange) and away (blue) from iron-vacancies using the same procedure as described above. Fourier transforming the two regions separately shows that in the near iron-vacancy region there is a weak dispersive hole band that is closing near 10 meV (Fig. 4.11g). In the region away from iron-vacancies, the image is dominated by the strong non-dispersive signal. The intensity of these two maps were scaled so that the sum of their q-integrated intensity is closest to that of Fig. 4.11d. This can be further demonstrated by looking at the fits to the peaks in line-cuts from Fig. 4.11g,h. For details of the fitting procedure see Appendix A.

Rotational Symmetry Analysis

To further investigate the translational-symmetry breaking modulation in $FeSe_{1-x}S_x$ we can analyze its local rotational-symmetry. Fig. 4.12a shows the real-space dI/dV at 6 meV where the strength of the modulation is strongest. The zoomed in and filtered image in panel b already indicate that the modulation is comprised of alternating stripe domains. We can separate the map in panel a into regions where the modulation wavevector is primarily along the q_a direction or primarily along the q_b direction, for the detailed procedure see Appendix

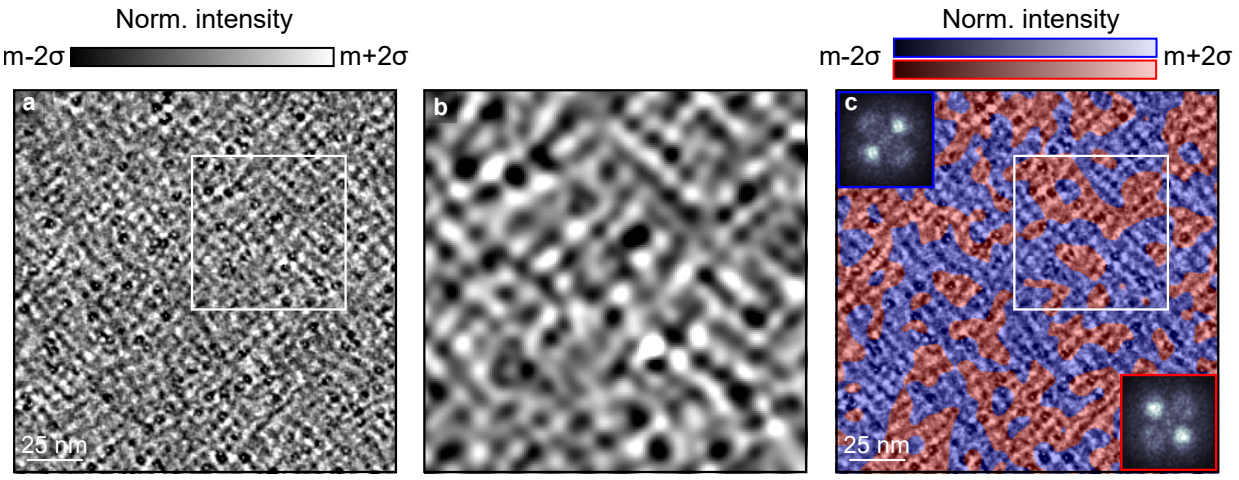

Figure 4.12: **a** dI/dV map measured on a $FeSe_{0.81}S_{0.19}$ sample at 6 mV. **b** Magnified view of the region marked by the square in a. The image is filtered to highlight the local structure of the 0.12 $Å^{-1}$ modulations. **c** The image in **a** overlaid with red and blue transparent masks that indicate regions of charge density wave only along a or only along b. The insets show the FTs over the two distinct regions under the red and blue masks. **d** Map indicating the domain boundaries between the red and blue regions (white) with locations of iron-vacancies overlaid (orange).

A. Fourier transforms of these two regions separately show two-fold symmetric peaks which are rotated by 90°, confirming that each region is comprised of a $q = 0.12\,Å^{-1}$ primarily along a single direction. This indicates that the electronic modulation, while being four-fold symmetric on average, is composed of small domains of two-fold symmetric stripes which are 90° rotated from one another.

Defects are known to pin fluctuations to form static orders and form domains. To this end, we investigated the role of iron-vacancies in the formation of the stripe domains. We did this by comparing the locations of iron-vacancies with the locations of the stripe domain walls and defining a correlation strength. The domain boundaries have a near zero value in the map used to get Fig. 4.12 c, so to get the domain map shown in Fig. 4.6 the absolute value is taken, divided by the maximum value, and subtracted from unity. Now, unity indicates the position of domain boundaries. The location of FeVs was determined at an energy (+29 meV) where QPI is weak and the FeVs stand out as bright spots in the dI/dV maps. We identified any signal larger than 1.5 standard deviations above the mean value of

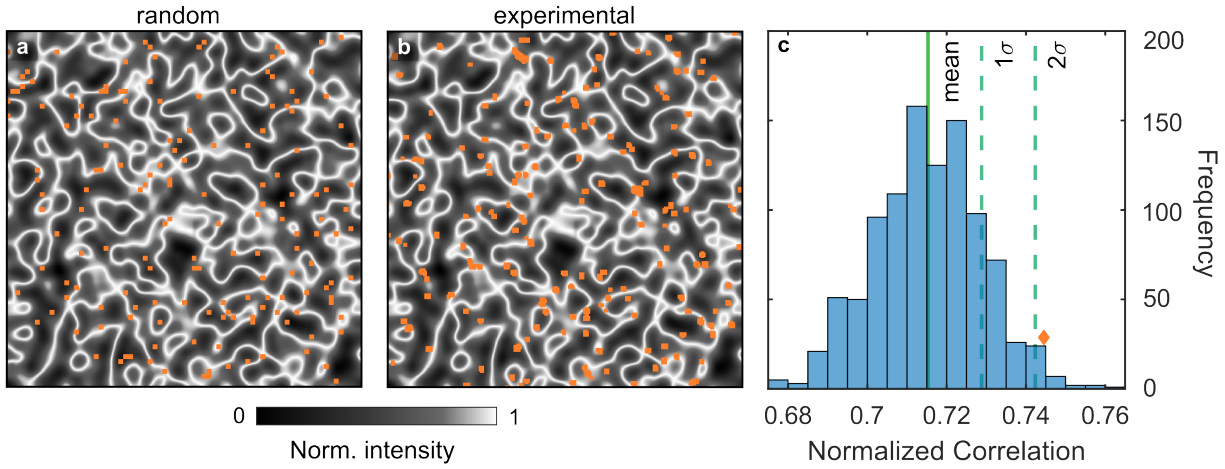

Figure 4.13: **a,b** Map showing the domain boundaries (white lines) from Fig. 4.12 with locations of FeVs overlaid (orange). Panel a shows a random distribution of FeVs whose correlation with domain boundaries is near the mean correlation, while in panel b the positions are determined experimentally at +23 meV. **c** Histogram of the correlation between the location of FeVs and the domain boundaries in Fig. 4.12d, obtained from 1000 simulated sets of 150 randomly located FeVs. The orange diamond indicates the correlation between the experimental iron-vacancy locations and the domain boundaries. The solid green line represents the mean of the distribution and the two dashed lines represent 1 and 2 standard deviations, σ.

the dI/dV as an FeV. Positions of FeVs were given a value of one, and zero was assigned elsewhere. We define a correlation strength between the locations of FeVs and domain boundaries via the product of their corresponding real-space maps. This correlation strength is then compared to the control parameter obtained by randomly placing impurities similar in size and quantity to what is found in our experiment. Doing this for 1000 trials of randomly located impurities, we find a distribution of correlation strengths (Fig. 4.6 c). We also find that the correlation strength from the experimentally determined FeVs locations is just over two standard deviations above the mean of this distribution. Fig. 4.6 a shows a random distribution of iron-vacancies whose correlation strength is near the mean. Since the iron-vacancies are concentrated near the domain boundaries, we conclude they are serving as local pinning sites.

Comparison to Charge Order in $Bi_2Sr_2CaCu_2O_{8+x}$

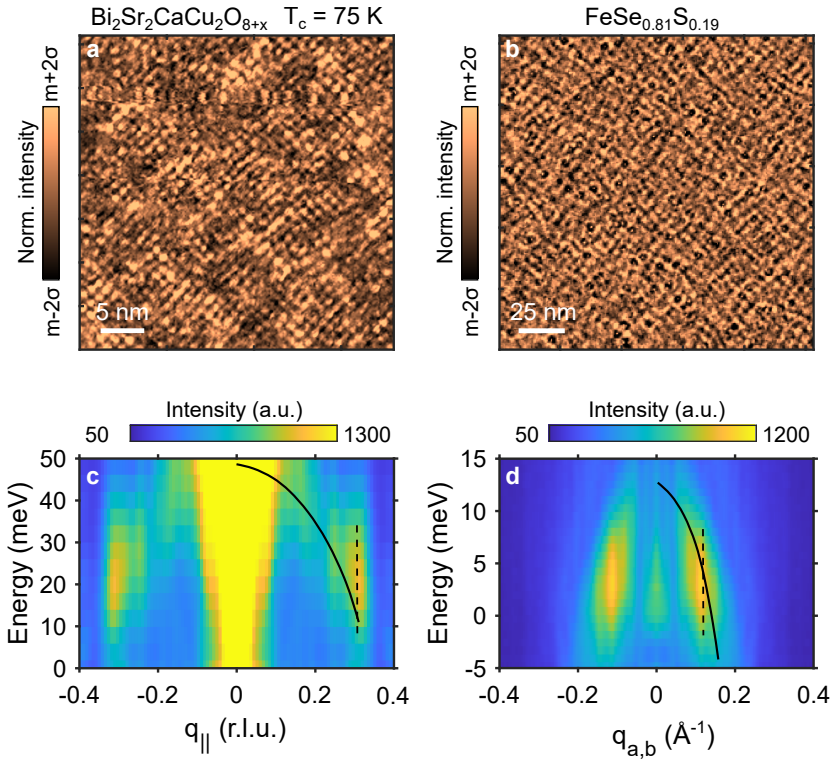

Figure 4.14: **a** Real-space dI/dV map of a cuprate superconductor $Bi_2Sr_2CaCu_2O_{8+x}$ with $T_c = 75\,\mathrm{K}$ at $+20\,\mathrm{meV}$. **b** Real-space dI/dV map at +6 meV on $FeSe_{0.81}S_{0.19}$. **c** Energy-momentum structure of the modulations obtained from the FTs of dI/dV measurements on $Bi_2Sr_2CaCu_2O_{8+x}$with $q_{||}$ along the Cu-O bond direction. **d** Energy-momentum structure of the modulations along the smallest Fe-Fe direction, $q_{a,b}$ obtained from the FTs of the measured dI/dV maps. Solid and dashed black lines are guides to the eye highlighting the dispersive and non-dispersive features, respectively. For more details on the data in **a** and **c**, see Ref. [64].

The phenomenology of the strong, non-dispersive feature is remarkably similar to that of broken-symmetry states in cuprate superconductors where the existence of a stripe-like charge ordering (CO) state is well established. Fig. 4.14 shows that, while the length and energy scales are different, the same three phenomenological features appear in both materials: (i) the real-space dI/dV appears as an alternating pattern of uni-directional stripes (ii) the energy momentum structure has an intense feature at finite **q** which does not disperse with energy (dashed black lines), and (iii) this non-dispersive feature appears at an energy

and wavevector that overlaps with dispersive QPI (solid black lines).

4.7 Discussion

With the help of our ARPES informed LDOS calculations and novel analysis techniques, we were able to successfully explain most features in the STS energy-momentum structure as QPI related to the band structure. One striking feature remained unaccounted for, and required additional investigation: the high intensity, non-dispersive peak just above the Fermi level. Next we will explore possible origins for the unexplained feature.

Smectic ordering in FeSCs with different periods and coherence lengths have been reported by STM/S in two other situations: LiFeAs under external uniaxial stress [65] and ultra-thin (one and two monolayers) FeSe films on $SrTiO_3$ [66, 67]. In both cases the underlying crystal structure already breaks rotational symmetry, indicating that a C_2 symmetric lattice may be necessary to foster the formation of the stripes. Our results shown in Figure 4.12 do indicate an underlying inhomogeneous uniaxial strain field is present in $FeSe_{0.81}S_{0.19}$. However, since the QPI emanating from the iron-vacancies is four-fold symmetric, it is possible that the rotational-symmetry breaking order couples more strongly with the translational-symmetry breaking state than it does with the electronic states in general. This seems to rule out a lattice driven rotational-symmetry breaking, which should effect the symmetry of QPI as well. Recent theoretical work has shown that defects on the surface can push the wave vector of the nematic state to a non-zero value, resulting in an electronic smectic phase at the surface [68]. While they only compare their calculations to the smectic state found in [68], which has a smectic wave vector two orders of magnitude smaller than ours, perhaps it is possible that for $FeSe_{0.81}S_{0.19}$ a larger wave vector does allow for a reasonable defect potential.

Theoretical studies of the effect of pressure on FeSe show a diverging electron compressibility, which indicates an instability towards either a phase separation or incommensurate

charge ordering [69]. Since the addition of sulfur is thought to suppress electronic correlations [21, 70], it is possible that sufficient sulfur substitution would push the system into the region of diverging compressibility, pointing to a charge order instability in $FeSe_{1-x}S_x$. A charge ordering state would also explain the experimental findings in this work, since we observe a modulation of the electronic charge density near the Fermi level, which does not disperse in energy. One peculiarity of the phase diagram of $FeSe_{1-x}S_x$ is that the maximum of T_c occurs well within the nematic phase, which contrasts with the prototypical Fe-based superconductors and suggests there is something in the vicinity of the nematic transition which is suppressing superconductivity. Charge order is well known in the cuprates to do exactly that. The comparison of the electronic stripes of $FeSe_{1-x}S_x$ to the charge order in $Bi_2Sr_2CaCu_2O_{8+x}$ in the previous section also support a charge ordering scenario in tetragonal $FeSe_{1-x}S_x$.

In addition to the discovery of electronic stripe patterns in tetragonal $FeSe_{1-x}S_x$, this work also introduces a new analysis technique which has the power to uncover scattering features which have been obscured due to disorder. This technique could be applied to other materials whose parent compound have well-known and well-defined scattering centers and whose QPI features suffer from broadening upon doping. Since chemical substitution is a common way to access new phases, this can become an essential analysis tool in STM/S on quantum materials.

Chapter 5

Study of Charge Order in a La-Based Cuprate

This work was done in collaboration with Timothy Boyle, Alejandro Ruiz, Zitong Zhao, William Moore, Santiago Blanco-Canosa, Alex Frano, Eduardo da Silva Neto, Fabio Boschini, Andrea Damascelli, Enrico Schierle, Ronny Sutarto, Teak Boyko, Feizhao He, Nobomichi Tamura, Christian Schussler-Langeheine, Eugen Weschke, Adrian Gozar, Alexander Komarek, and Wei Peng. The measurements were taken over at least four weeks of beamtimes between the Canadian Lightsource and BESSY-II. Timothy Boyle designed and constructed the strain device. Timothy Boyle, Alejandro Ruiz, Santiago Blanco-Canosa and I carried out the resonant x-ray scattering measurements and preliminary analysis under the supervision of Alex Frano and Eduardo da Silva Neto. The beamline scientists Enrico Schiele, Christian Schussler-Langeheine, and Ronny Sutarto all assisted in measurements, including significant modifications to their scattering chambers to accommodate the strain device. Zitong Zhao and William Moore performed the COMSOL simulations. Alexander Komarek and Wei Peng synthesized the $La_{1.475}Nd_{0.4}Sr_{0.125}CuO_4$ crystals. These results have been published in Physical Review Research [71].

5.1 Introduction

Superconductivity in the cuprates was first discovered in $La_{2-x}Ba_xCuO_4$ (LBCO) in 1986 by Bednorz and Mueller [4]. The 30 K transition temperature was higher than was thought possible according to BCS theory, pointing to an unconventional superconductivity. This record T_c was quickly surpassed the following year when superconductivity was found in $YBa_2Cu_3O_{6+y}$ at 93 K [5]. Mountains of experimental and theoretical work have led to

the conclusion that the superconducting pairing symmetry is d-wave, however the pairing interaction is still debated [52]. The search for the pairing mechanism necessitates an understanding of neighboring and overlapping exotic phases, such as antiferromagnetism, electronic nematicity, and charge order. This work will focus on the charge order in the La-214 curpate $La_{1.475}Nd_{0.4}Sr_{0.125}CuO_4$.

Charge order in the cuprates was first discovered in $La_{1.475}Nd_{0.4}Sr_{0.125}CuO_4$ using neutron scattering [9], and shortly after found in the rest of the La-based cuprates [72, 73]. The charge order was originally thought unique to the La-214 cuprates, but STS studies Bi-2212 revealed real-space modulations of the LDOS that were eventually determined to be due to charge order [74]. STS studies alone were not enough to conclude the charge order origins in Bi-2212 because the modulations were weak and short-ranged and the studies were not sensitive to the bulk electrons. Improvements to resonant soft x-ray scattering allowed the discovery of long-range charge order correlations in YBCO [75], and the detection of the charge order peak in Bi-2212 [64], and then in all cuprates which solidified charge order as a universal phenomenon in the cuprates [26].

La-based cuprates of the form $La_{2-x}M_xCuO_4$ where M is a rare-earth metal such as Ba, Sr, Nd, or Eu, known as the "214" family, have several electronic orders in the vicinity of superconductivity. Figure 5.1a shows a schematic phase diagram of temperature and doping for this family of superconductors. The ground state is antiferromagnetic, and the normal state is a strange metal. In between is the superconducting dome which has an anomalous depression at 1/8 hole doping, known as the 1/8 anomaly. In the region just around the 1/8 anomaly is a stripe-like charge order state. The charge order occurs as two-dimensional stripes in the copper oxide planes, with each layer alternating directions. While in three dimensions the charge order is overall tetragonal, within each CuO_2 layer it is two dimensional.

Additionally, these materials undergo successive structural transitions as temperature is lowered. At high temperatures the system is tetragonal (HTT), undergoes a low tempera-

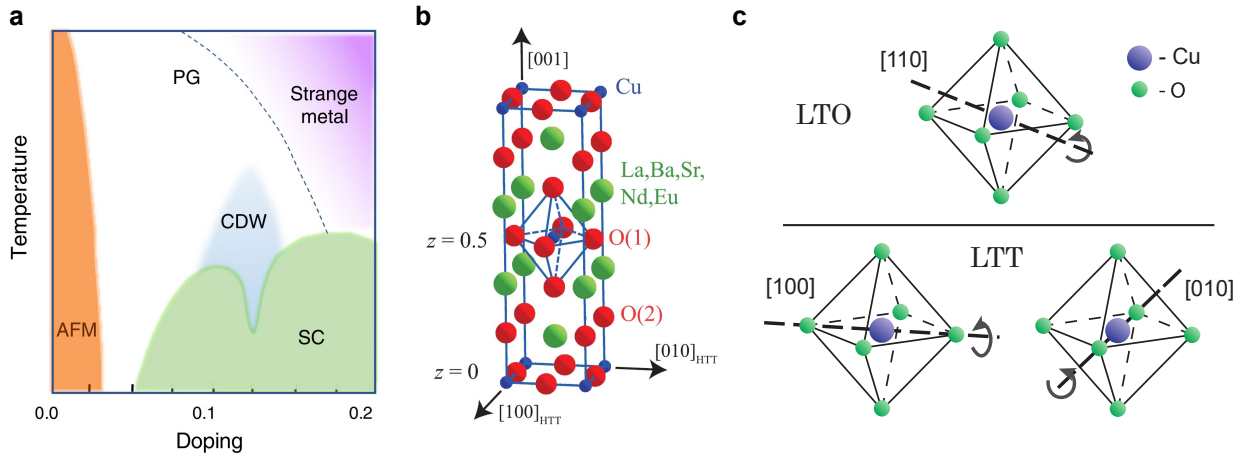

Figure 5.1: **a** Schematic phase diagram for the La-214 cuprates reproduced from [76]. **b** Crystal structure of the La-214 cuprates in the HTT state reproduced from [77]. **c** A diagram depicting the CuO_6 octahedral tilts in both the LTO and LTT phases. In the LTO phase, neighboring octahedra tilt in opposite directions (clockwise and counter-clockwise) along the [110] direction. In the LTT phase, adjacent CuO_2 layers have orthogonal tilts along the [100] and [010] directions. **a-c**

ture orthorhombic (LTO) transition, and then finally undergoes low temperature tetragonal (LTT) transition. These structural transitions are understood as tilts of the CuO_6 octahedra that are situated between layers of the rare-earth metals (see Fig. 5.1b). In the HTT there is no tilt of the octahedra. In the LTO state the octahedra tilt about an axis 45° from the Cu-O bond direction (See Fig. 5.1c). In the LTT state the octahedra within a single layer all tilt about an axis parallel to the Cu-O bond directions, but this tilt axis alternates between neighboring layers. Thus, the crystal structure is globally tetragonal.

The charge order in the "214" family is strongly coupled to the LTT phase, which is thought the stabilize the charge order fluctuations into the static state [78]. Resonant x-ray scattering can probe both of these phases. The (001) Bragg peak is forbidden in the HTT phase due to high symmetry along the c-axis. However on resonance, the symmetry that matters when determining the selection rule is that of the specific element the photon energy is tuned to. The tilting of the octahedra can alter the chemical environment even when it does not break the overall lattice symmetry. In the LTO phase the Cu-O planes are not rotated between layers, only shifted, which does not break the c-axis symmetry. After the

LTT transition the Cu-O planes of neighboring layers are rotated by 90°, which does break the symmetry along the c-axis. Thus in the LTO state the (001) peak remains forbidden, but in the LTT state it is restored, allowing the presence of the (001) Bragg peak to be an indication of the LTT transition [79]. The intensity of the (001) is also a measure of the octahedral tilt angle, which evolves smoothly through the transition and this evolution depends on which rare-earth element is sitting in the La sites [80, 79].

External tuning parameters such as magnetic field and hydrostatic pressure have been shown to alter the interplay between these exotic phases. For example, hydrostatic pressure applied to $La_{2-x}Ba_xCuO_4$ entirely suppresses the LTT transition while charge order sees a moderate reduction in transition temperature [78]. More recently, application of uniaxial strain has been shown to alter both superconductivity and charge order in other La-based cuprates. In this experiment we applied uniaxial strain applied along on of the Cu-O bond directions to see the effect on both the charge order and the structural transition to the LTT phase. If the charge order were coupled perfectly to the LTT phase, one would expect the two orders would experience the same effect due to strain. However, if the connection between the two is more complicated, such as the involvement of another order, they might be changed differently. Additionally, the uxiaxial strain may cause a difference between the charge order along the direction of applied strain and along the direction perpendicular to strain. We used resonant x-ray scattering to measure the intensity of the charge order as a function of temperature and to track the LTO-LTT transition via the (001) Bragg peak on both strained and unstrained samples of $La_{1.475}Nd_{0.4}Sr_{0.125}CuO_4$. In $La_{1.475}Nd_{0.4}Sr_{0.125}CuO_4$ (LNScharge order-125), which is near the 1/8 anamoly, superconductivity is suppressed to near 5 K, and $T_{CO} \approx T_{LTT} \approx 75$ K. The wavevector of the charge order is $\mathbf{q} = 0.23$ r.l.u..

5.2 Experimental setup

We performed resonant x-ray scattering experiments at two different beamlines: UE-46-PGM1 at BESSY II and 10ID-2 (REIXS) at the Canadian Light Source; additional experiments were carried out at beamline UE-56/2-PGM2 of BESSY II using the Resonant Scattering Station and beamline 12.3.2 (microdiffraction) at the Advanced Light Source. Measurements done at UE-46 we all taken with a point detector (photodiode), while measurements at the REIXS beamline also had the advantage of a two-dimensional detector. Both beamlines had motor control for all three sample position axes, as well as motors for at least two sample angles, and the detector angle. The single crystals were synthesized by floating zone and previously characterized by means of resonant x-ray scattering and magnetometry [81].

Strain device

One sample was glued across a gap in a titanium horseshoe-shaped device (Fig. 5.2a) following the design of Hicks et. al. [82]. The device consists of four main components: a titanium U-frame, three piezoelectric stacks (piezo stacks), a titanium base, and two titanium sample holder pieces. Glued on the outer ends of the U-frame are two piezo stacks while the other end of the stacks are glued to the base. In the middle of the base a third piezo stack is attached which has a sample holder piece glued to it. This sample holder piece is not directly connected to the U-frame. The second sample holder piece is attached to the center of the U-frame. The sample is mounted with a strong epoxy in the gap between the sample holder pieces. The sample holder pieces are removeable to make each device reusable and their positions adjustable to accommodate varied sample dimensions. Another sample was glued to the titanium faces of the U-frame. The device was designed to apply strain by applying voltage of opposite polarity to the inner and outer piezo stacks. The devices were tested at room temperature using the micro-Laue diffraction beamline. The results of this

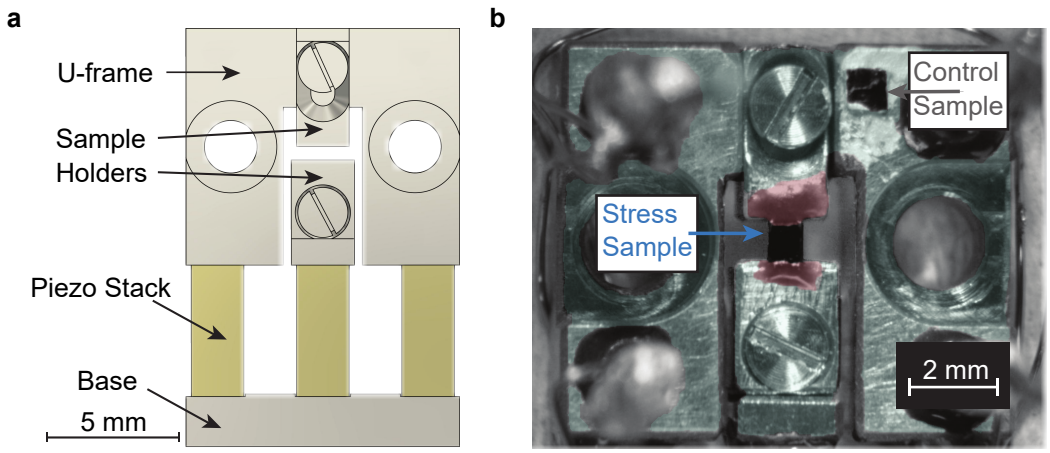

Figure 5.2: **a** A schematic diagram of the strain device. **b** An image of the titanium strain device and LNSCO-125 crystals. The stress sample is mounted in the center across a gap using a stiff epoxy and the control sample is mounted on the titanium using silver paint.

test indicated that the strain was uniform across the center of the sample and the maximum strain applied at room temperature was 0.3%.

Sample mounting and orientation

Both samples were mounted and oriented so the c-axis is out-of-plane and the a-axis is along the direction of the gap. The samples were first positioned in the x-ray beam using a camera, and then the positions of the sample mapped out by measuring the fluorescence as a function of position. The measurement position was chosen to be in a region near the center of the sample that had good intensity and was uniform. The orientation of the sample was determined first by finding an out-of-plane Bragg peak and correcting for any flip angle offsets, and then by finding a in-plane Bragg peak. The absorption edges were determined by performing x-ray absorption spectroscopy scans, which had to be done using total fluorescence yield because the strain device does not allow measurement of the drain current. The alignment of samples and tuning of the photon energy was checked periodically and after large changes in temperature.

Data collection and analysis

The charge order (CO) scans were collected as rocking curves with the detector at a fixed angle of $2\theta \approx 148$ degrees, corresponding to $L \approx 1.7$ (r.l.u.) at the peak position using a photon energy tuned to the Cu L_3-edge (931.5 eV). 3 to 10 charge order scans were taken at each temperature depending on the intensity of the peak being measured, with weaker peaks requiring longer counting to achieve the desired statistics. After changing the temperature, at least 5 minutes were allowed for the temperature to stabilize before beginning data acquisition. Scans of the (001) Bragg peak were collected also using rocking curves with the photon energy tuned to the O K-edge (532.5 eV).

The profile of the background of each rocking curve is subject to several systematic effects, including the angular dependence of the fluorescence background emission and the projection of the incoming photon beam onto the sample surface. To mitigate this systematic error, scans at each temperature were averaged 3 to 10 times, with measurements of the high-temperature charge order correlations requiring greater statistics; these sets of measurements typically took 2 hours each. The averaged scans were vertically shifted and had a linear slope subtracted to best match the background profile of a fourth-degree polynomial fit of a high-temperature background curve (see dashed line in Fig. 5.3b). The high-temperature background fit was then subtracted from each curve, and the resulting peaks were fit to a Lorentzian function. When peak intensities are plotted, the value shown is that from the Lorentzian fit.

5.3 Results

Observation of precursor charge order (PCO) up to 200 K

First we measured the intensity of the charge order on an unstrained sample from 10 K to 300 K (Fig. 5.3a). The charge order peak is centered at $\mathbf{q}_{||} = 0.23$ r.l.u. and is most intense at 10

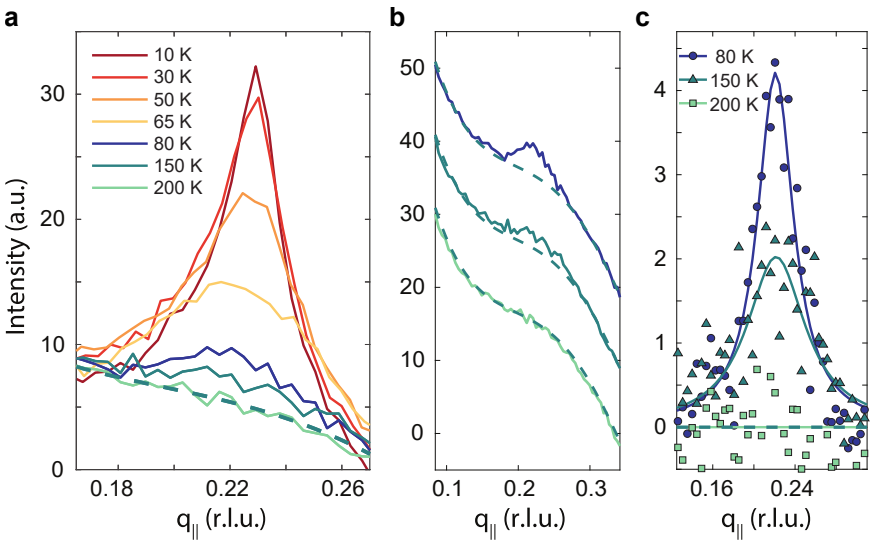

Figure 5.3: **a** Temperature dependence of the charge order peak in unstrained LNSCO-125. Sharp peaks corresponding to charge stripes are observed below 65 K in the LTT phase. The green dashed line is a polynomial fit of the high-temperature background curve measured at 300 K. **b** RXS scans in the LTO phase showing broad peaks corresponding to charge order correlations. **c** Lorentzian fits of the background-subtracted curves shown in **b**.

K, and decreases with increasing temperature. While the intensity of the charge order drops significantly in above T_{LTT} = 63 K, a small peak still persists and is not fully suppressed until 200. This can best be seen in Fig. 5.3b, which shows the same data as in a, but only for high temperatures and with vertical offsets . Figure 5.3c shows these curves but with the fit to the high temperature background subtracted and also shows a fit to a Lorentzian peak. We attributed this peak above the T_{LTT} to charge order correlations which could be coming from either static or dynamic correlations. An energy resolved experiment would need to be performed to determine whether the correlations are static or dynamic.

Applying and quantifying strain

We determined the amount of stress applied by tracking the (103) Bragg peak of both the control and strained sample to determine the new lattice parameters under strain. Both the strain and control sample will experience a contraction of all lattice parameters when temperature is decreased, but only the strained sample will have a difference in contraction

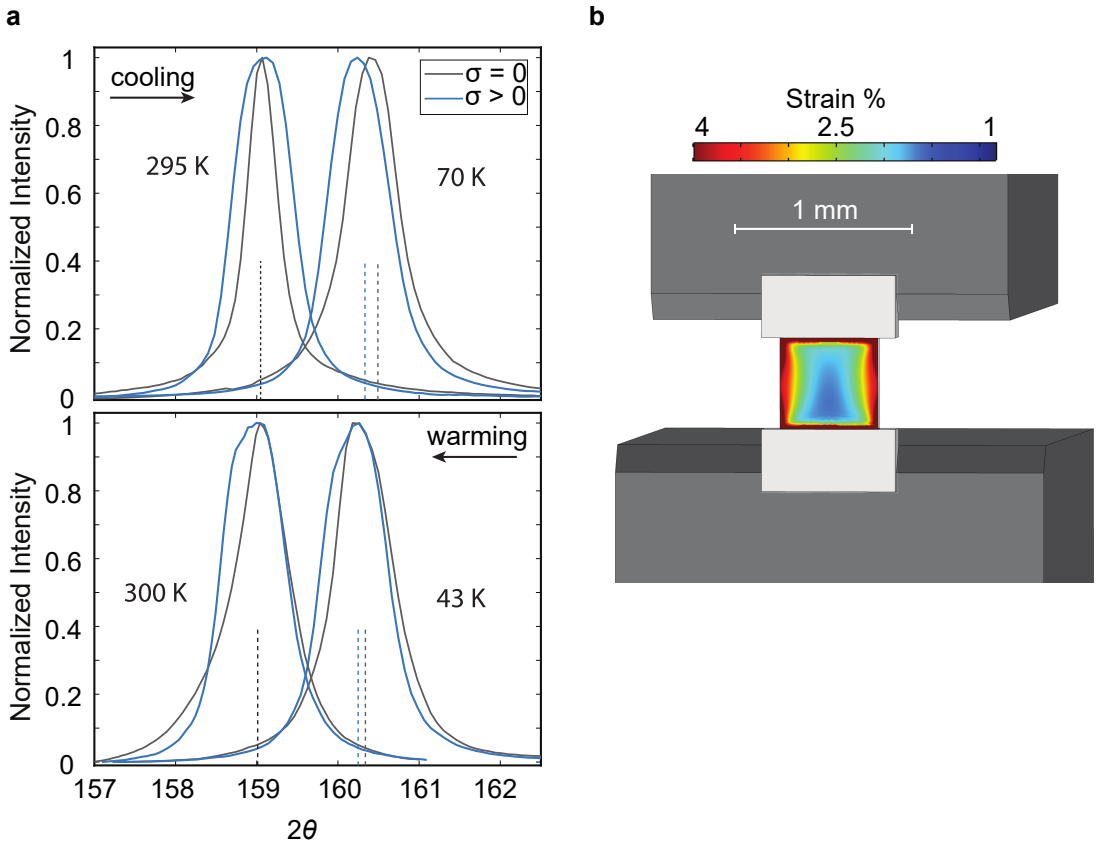

Figure 5.4: **a**(103) Bragg peaks of the control and stress samples at high and low temperatures. The smaller change in 2θ of the stress sample is a consequence of tensile strain. Measurements shown in the top panel were performed upon cooling and the bottom panel upon warming. The dotted lines indicate the center-of-mass positions of the peaks; black corresponds to the high temperature positions and blue and gray correspond to the low temperature positions of the stress and control samples respectively. **b** A COMSOL Multiphysics® model of the strain device at 70 K showing a tensile strain pattern on the surface of the sample. The titanium sample holders are dark gray and the epoxy is light gray.

along the strained vs. unstrained axis. We tracked the (103) Bragg peak at high and low temperature by performing θ-2θ scans with a photon energy of 2200 eV. This was done before and after cooling the sample at the beginning of the experiment, and finally before and after warming the sample at the end of the experiment. These scans are shown in Fig. 5.4a. Upon cooling to $T = 70$ K, we observed a difference of $\Delta 2\theta = 0.145$ degrees in the center-of-mass position of the peaks of the stress and control samples at low temperature, indicating that strain is already applied due to differential thermal contraction. Upon warming we observed $\Delta 2\theta = 0.045$ degrees. This yields average difference of 0.095 ± 0.05 degrees in 2θ, which

corresponds to a difference in the change of the in-plane lattice constant of $0.046 \pm 0.026\,\%$. Using $C_{11} = 232$ GPa for the elastic modulus, this corresponds to a strain of $\sigma = 0.11 \pm 0.06$ GPa. At low temperatures we were not able to see any change in the Bragg peaks due to voltage applied to the piezo stacks. There are several possible reasons no discernible strain was applied by applying voltage to the piezo stacks, including the strong temperature dependence of the piezoelectric effect and sample geometry. Previous experiments applying *in situ* strain using piezo devices used thin, needle-like samples with the long axis along the strain direction [83, 84], while our samples had large cross-sectional area. Nonetheless, it turns out the strain applied via differential thermal contraction was sufficient for the purpose of this experiment. The sample and titanium device contracted less than the epoxy, resulting in a net tensile strain along the sample a-axis.

Table 5.1: Values for the Young's modulus (Y) and coefficient of thermal expansion (α) used in our COMSOL simulation. Values for the H74F epoxy came from EPO-TEK® H74F Product Information Sheet. Values for titanium came from the COMSOL Material Library. The value for α for LNSCO-125 was obtained from the Bragg peaks of the control sample and are consistent with values reported for LSCO [86]. The Young's modulus of the epoxy was increased by a factor of 6 (from $4 \cdot 10^9$ Pa to $2.4 \cdot 10^{10}$ Pa) at 70 K to be consistent with the temperature dependence reported for other epoxies [87].

	H74F Epoxy	LNSCO-125	Titanium
Y	$2.4 \cdot 10^{10}$	$2.5 \cdot 10^{11}$ [85]	$1.161 \cdot 10^{11}$
α	$2 \cdot 10^{-5}$	$5.02 \cdot 10^{-6}$	$6.51 \cdot 10^{-6}$

We also performed multiphysics simulations using the thermal and elastic properties and realistic geometry of the sample in the strain device and got comparable results. To simulate the stress produced by the strain device we construct a COMSOL Multiphysics® model, shown in Figure 5.4a. This simulation incorporates both the elastic moduli and coefficients of thermal expansion of the titanium, epoxy, and LNSCO-125 crystal, as well as the arrangement of the sample and epoxy within the gap. We observe a net tensile-strain pattern across the top surface of the sample at 70 K with an average value of 0.0294%, which is of the same order of magnitude as measured by the BPs. Table 5.1 lists the parameters for Young's modulus (Y) and the coefficient of thermal expansion (α) of the different materials

in the simulation.

Effect of strain on (001) Bragg peak

Figure 5.5 shows the integrated intensity of the [001] Bragg peak as a function of temperature for both the strained and unstrained samples. On the unstrained control sample, the intensity of the (001) Bragg peak begins to rise around 70 K, and shoot up sharply with $T_{\mathrm{LTT}} = 63$ K and begins to saturate around 40 K. On the strained sample, there is no significant intensity of (001) Bragg peak until below 40 and T_{LLT} is reduced by 29 K to 34 K. The intensities of the peak in both samples saturate to around the sample value. The external stress causes a preferred Cu-O direction, making it more difficult to achieve a globally tetragonal phase. As temperature is lowered further, the lattice mismatch finally overcomes external strain and the LTT phase does emerge. This result demonstrates that a very modest amount of strain can dramatically alter the structural transitions. Other groups have hypothesized that uniaxial strain could cause a change in the octahedral tilt angle of the LTT phase, or induce regions of LTO in some areas of the sample. Note that the transition is very sharp even for the strained sample, though slightly broader than in the unstrained sample. This indicates that a fully LTT phase is realized and we are not likely observing some mixed LTO-LTT state.

Effect of strain on charge order

Next we looked at the effect of strain on the charge order. Figure 5.6a shows the integrated intensity of the charge order peak as a function of temperature for the unstrained sample (gray), and for the strained sample along the direction parallel to (blue) and perpendicular to (orange) the applied strain. First note that between the unstrained and strained sample, T_{CO} decreased by 50 K, which is an even larger change that was seen in T_{LTT}. Second, in the unstrained sample charge order onsets before T_{LTT}, while for both strained samples the onset of charge order is pushed below T_{LTT}. There is a small difference in the onset of charge order

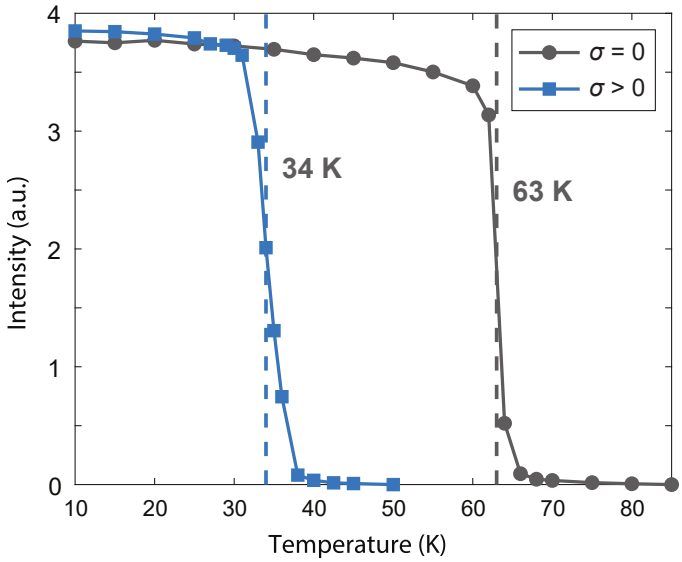

Figure 5.5: Temperature dependence of the (001) Bragg peak on the apical O-K edge in both the stress and control samples corresponding to the LTT phase transition. The transition temperature is suppressed by 29 K with the applied stress.

in the strained samples depending on the direction of applied strain. The charge stripes in the direction of applied strain onset before those in the perpendicular direction by about 6 K. Finally, our measurements show no discernible difference in the PCO along the two direction.

5.4 Discussion

Using resonant x-ray scattering tuned to the Cu L_3-edge we have measured the charge order peak in $La_{1.475}Nd_{0.4}Sr_{0.125}CuO_4$ for both strained and unstrained samples. We have shown that a precursor charge order PCO, which is already established in $La_{2-x}Ba_xCuO_4$ and other cuprate systems, is present in $La_{1.475}Nd_{0.4}Sr_{0.125}CuO_4$ as well. Our measurements with uniaxial strain along one of the Cu-O bond directions show a dramatic reduction of both T_{LTT} and T_{CO} by 29 K and 50 K, respectively. The charge order measured along the direction of applied strain saw a larger reduction of T_{CO} the did the charge order along the perpendicular direction by 6 K. Within the resolution of our experiment, the PCO is not affected by the

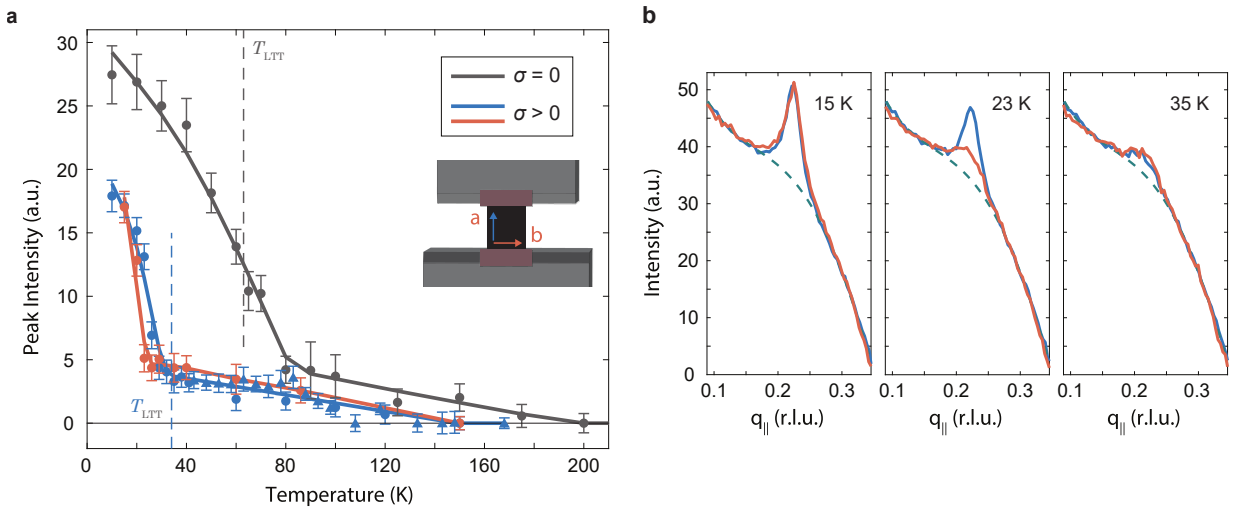

Figure 5.6: **a** Temperature dependence of the charge order peaks in the stress and control samples. The solid lines serve as guides to the eye. The dashed lines correspond to the LTT transition temperatures determined from Fig. 5.4 The inset shows a diagram of the stress sample, where we label a (blue) and b (orange) as the directions parallel to and perpendicular to the direction applied stress respectively. Measurements of the stress sample along the a direction were performed at two different synchrotrons: measurements from the Canadian Light Source are triangles and measurements from BESSY-II are circles. **b** Comparison of stress sample RXS scans along the a and b directions near the LTT transition. The gray dashed line is a polynomial fit of the high-temperature background curve measured at 150 K. The onset of the charge stripes along the direction of applied stress precedes that of the perpendicular direction by approximately 6 K.

applied uniaxial strain.

Charge fluctuations before the formation of static stripes have been observed before in several cuprate systems [76, 88]. Because our experiment is energy-integrated, it is impossible to determine if the precursor charge order (PCO) is due to static or dynamical correlations. One also cannot assume that the PCO has the same rotational symmetry as the static charge order. In fact, the dynamic charge order correlations in $Bi_2Sr_2CaCu_2O_{8+x}$ are present at $\mathbf{q}_{CO}$ along all direction in the copper oxide plane while the static charge order appears only in the Cu-O bond direction [89]. This could explain our observation that there is no direction-dependent effect of the PCO due to strain, while for the static charge order there is.

One would expect that if there were a one-to-one coupling between the LTT phase and the charge order, any modification of one phase would would be reflected in the other. This

is not what we see. While uniaxial stress reduced T_{LTT} by 29 K, it reduced the charge order transition before 50 K. This indicates that some other order, such as superconductivity, is also influencing the phases we measured. Our experiment did not allow for simultaneous probing of T_{c}, but other experiments have shown that comparable amounts of uniaxial stress enhances T_{c} in similar systems [90, 91]. Since superconductivity and charge order are known to compete in these systems, the strain could be further suppressing the charge order via enhancement of the superconductivity.

Overall, the observation of PCO in $La_{1.475}Nd_{0.4}Sr_{0.125}CuO_4$ is further evidence that the phenomenon is universal in the cuprates. Investigations using RIXS to determine if these charge fluctuations are static or dynamic and to determine their momentum dependence are underway. Additionally, our results on the effect of strain on the LTT transition and charge order show that only small amounts of strain are needed to dramatically alter the electronic states of $La_{1.475}Nd_{0.4}Sr_{0.125}CuO_4$. Bringing additional interest is the difference in effect seen in the LTT phase and the charge order phase. Further experiments probing the effect of strain on the superconductivity are necessary since it is clear superconductivity must be taken into account to explain our current findings.

Chapter 6

Conclusions

Broken-symmetry states in proximity to the superconducting state in two unconventional superconductors were studied using modern spectroscopies. In the iron-base superconductor $FeSe_{0.81}S_{0.19}$, a new electronic stripe pattern was observed using scanning tunneling spectroscopy (STS). In cuprate superconductor $La_{1.475}Nd_{0.4}Sr_{0.125}CuO_4$, we probed the interplay between charge order and the low temperature orthorhombic to tetragonal transition by straining the material and measuring the response with resonant x-ray scattering. Both studies represent a piece in the overall puzzle of interactions between electrons in unconventional superconductors. For updates on follow up work to these studies, look to the dissertation of Kirsty Scott at Yale University.

Our STS measurements and new scatterer-resolved QPI procedures advance the detection of QPI and broken-symmetry states and the ability to distinguish between the two. Our ARPES calibrated QPI simulations successfully account for almost all scattering features revealed in our STS dispersion maps. However, just above the Fermi level there is one intense feature along the shortest Fe-Fe directions and centered at $\mathbf{q} = 0.12$ Å^{-1} that remains unaccounted for. After applying the scatterer-resolved QPI technique to higher resolution measurements of this feature, it is apparent this feature does not disperse for approximately 10 meV. Analysis of the real-space image reveals short-range electronic stripe patterns with a wavelength that corresponds to the wavevector of the non-dispersive signal. Because the QPI patterns remain four-fold symmetric, the origin of these stripes must be different than the well known nematic state. Altogether, these electronic stripes remind us of the phenomenology of the charge order in Bi-2212, indicating their origin may be

related to incipient charge order correlations. Further studies on the electronic stripes in $FeSe_{0.81}S_{0.19}$ are still needed. A bulk charge order state could be confirmed using resonant x-ray scattering, as was done for Bi-2212 [64]. Preliminary experiments searching for bulk charge order proved to be challenging. Coupling of the stripes to the lattice can be tested by applying *in situ* uniaxial strain to see if it instills a preferred orientation. Progress to apply *in situ* strain during an STS experiment is nearing completion and with luck measurements will begin in the near future.

We used resonant x-ray scattering to probe the charge order and LTT transitions in cuprate superconductor $La_{1.475}Nd_{0.4}Sr_{0.125}CuO_4$. We first detected a precursor charge order peak at temperatures well above the static charge order transition. We then applied uniaxial strain and saw a dramatic reduction in the transition temperatures for both the LTT phase and the charge order. While the LTT transition was reduced by 20 K, the charge order transition saw a 50 K reduction. The decoupling of the two transitions indicates that the strain must be affecting an additional order such as superconductivity, which is known to compete with charge order and to be affected by strain in similar materials. The dramatic response of the electronic states to modest strain shows promise that strain can be a viable way to tune the electronic properties in switchable devices. A direction of future work is to measure the angular dependence of the precursor charge order. The static charge order occurs only in the directions of the Cu-O bonds, but in other systems with high-temperature charge order correlations they exist at the same $|\mathbf{q}|$ vector for all angles. Preliminary results support this scenario, and further measurements including more angles and with better resolution are ongoing.

Appendix A

Analysis notes to Chapter 4

This appendix serves to explain the details that went into producing some of the figures in Chapter 4 which were omitted in the main text for the sake of clarity.

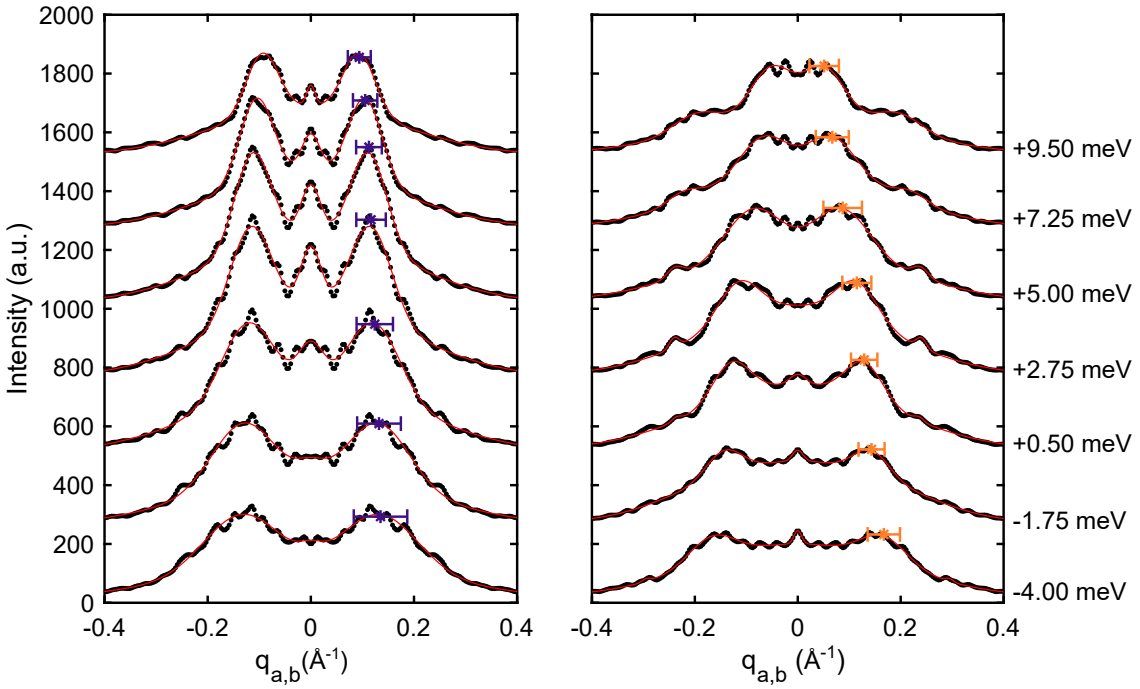

Figure A.1: Constant energy linecuts (black dots) from Fig. 4.11 at the energies indicated on the right of b. Red lines are fits of the data, blue and orange stars indicate the peak position extracted from the fit with estimated error.

Procedures for Fig. 4.11

Linecuts taken at the selected energies for the two regions were fitted with Gaussian peaks plus a small constant offset (Figure 4.11). The central area ($q \approx 0$) was fitted by one or two Gaussian peaks. To characterize the QPI features at finite q values we used two symmetric

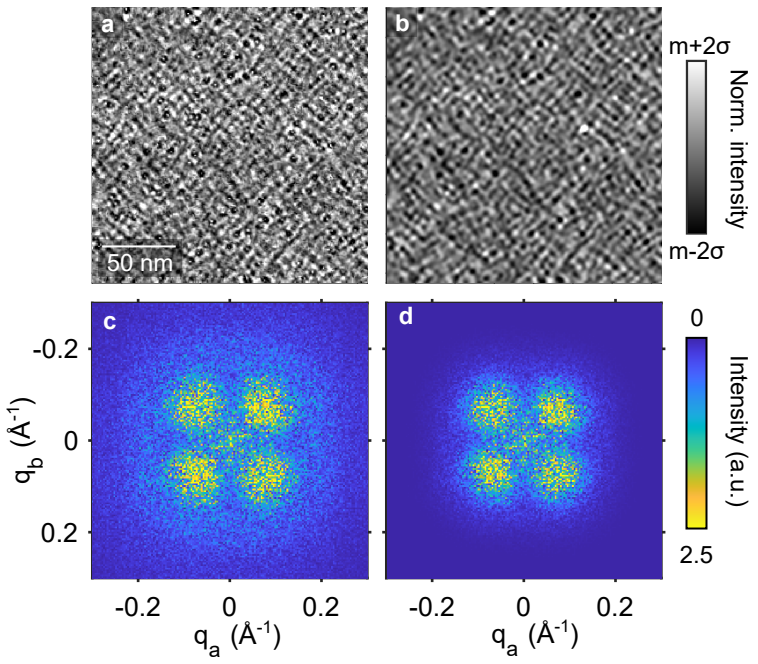

Figure A.2: **a**,**b** Raw and filtered dI/dV map on $FeSe_{0.81}S_{0.19}$ at 4 mV, normalized by the mean of the image. **c**,**d** Fourier transform of the images in **a** and **b** respectively. The filtered image is obtained by applying a Gaussian filter centered at the locations of the four peaks that compose the 0.12 $Å^{-1}$ modulations, as can be seen by comparing **c** and **d**.

peaks for the left panel and two additional peaks for the right panel to include the small intensity feature around $q \approx 0.23$.

Procedures for Fig. 4.12

Fig. 4.12b of the main text shows a dI/dV image of the stripe modulations after filtering. Figure A compares the filtered and unfiltered images of the entire scan area. The filter is applied in Fourier space and it is composed of four Gaussian peaks centered around the stripe peaks in Fourier transform of the original image.

In Fig. 4.12c we separated the map into regions where the $q = 0.12\,Å^{-1}$ are primarily along q_a or q_b. To do this, the original dI/dV image (Fig. Aa) is multiplied by a complex modulation with wavelength equal to the wavelength of the $q = 0.12\,Å^{-1}$ (Fig. Ab) electronic stripes in the q_a and q_b directions separately. This product (Fig. Ac) is Fourier transformed, multiplied by a Gaussian window and then inverse Fourier transformed back to real space. In this way

we obtain two spatial maps corresponding to the intensities of the these modulations along q_a and q_b (Fig. Ad-e). The intensity maps for the two directions are subtracted to get the red/blue domain map in Fig. 4.12c, where positive (negative) values indicating modulations primarily along q_b (q_a) are blue (red) (Fig. Af).

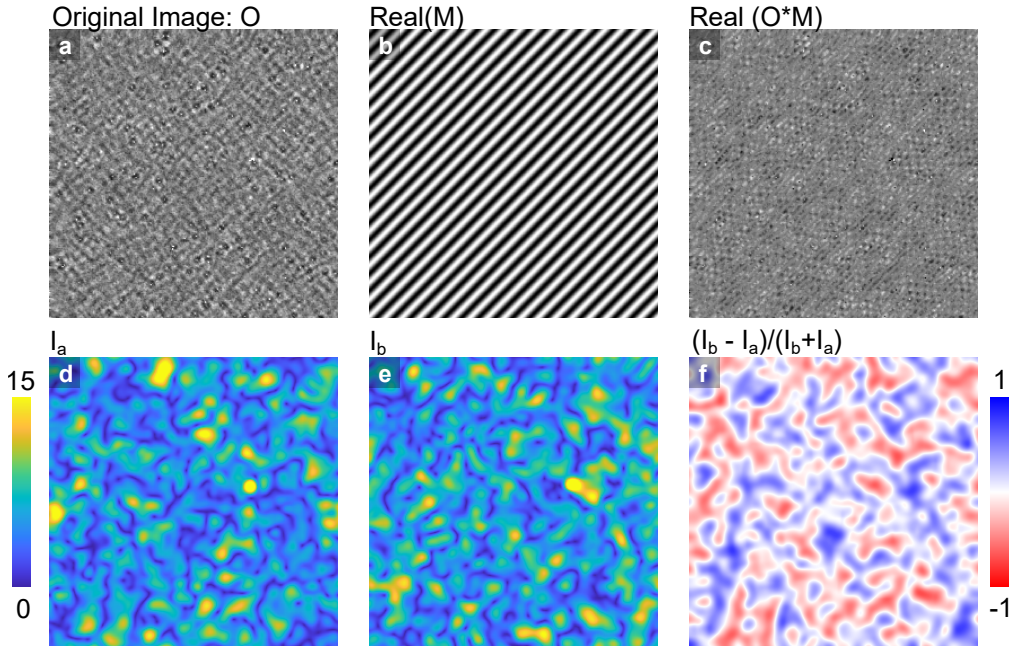

Figure A.3: **a** Original dI/dV map O on $FeSe_{0.81}S_{0.19}$ at 4 mV, normalized by the mean of the image. **b** The real part of the complex modulation along the a direction, M_a. **c** The real part of product of O and M. **d**,**e** Maps of the intensities of the local modulation along a and b, respectively. **f** The difference in intensities along a and b normalized by their sum.

Bibliography

[1] Bardeen, J. Nobel Lecture. www.nobelprize.org, Nobel Foundation (1956).

[2] Onnes, H. K. The Superconductivity of Mercury. *Commun. Phys. Lab. Univ. Leiden* 122–124 (1911).

[3] Bardeen, J., Cooper, L. N. & Schrieffer, J. R. Microscopic Theory of Superconductivity. *Physical Review* **106**, 162–164 (1957).

[4] Bednorz, J. G. & Mueller, K. A. Possible high Tc superconductivity in the BaLaCuO system. *Zeitschrift fur Physik B Condensed Matter* **64**, 189–193 (1986).

[5] Wu, M. K., Ashburn, J. R., Torng, C. J., Hor, P. H., Meng, R. L., Gao, L., Huang, Z. J., Wang, Y. Q. & Chu, C. W. Superconductivity at 93 K in a new mixed-phase Y-Ba-Cu-O compound system at ambient pressure. *Physical Review Letters* **58**, 908–910 (1987).

[6] Weijers, H. W., Kandel, H., Bai, H., Gavrilin, A. V., Viouchkov, Y. L., Larbalestier, D. C., Abraimov, D. V., Markiewicz, W. D., Voran, A. J., Gundlach, S. R., Sheppard, W. R., Jarvis, B., Johnson, Z. L., Noyes, P. D. & Lu, J. Progress in the Development of a Superconducting 32 T Magnet With REBCO High Field Coils. *IEEE Transactions on Applied Superconductivity* **24**, 1–5 (2014).

[7] Steglich, F., Aarts, J., Bredl, C. D., Lieke, W., Meschede, D., Franz, W. & Schäfer, H. Superconductivity in the Presence of Strong Pauli Paramagnetism: $CeCu_2Si_2$. *Physical Review Letters* **43**, 1892–1896 (1979).

[8] Machida, K. Magnetism in La_2CuO_4 based compounds. *Physica C: Superconductivity* **158**, 192 – 196 (1989). URL http://www.sciencedirect.com/science/article/pii/092145348990316X.

[9] Tranquada, J. M., Sternlieb, B. J., Axe, J. D., Nakamura, Y. & Uchida, S. Evidence for stripe correlations of spins and holes in copper oxide superconductors. *Nature* **375**, 561–563 (1995).

[10] Loeser, A. G., Shen, Z.-X., Schabel, M. C., Kim, C., Zhang, M., Kapitulnik, A. & Fournier, P. Temperature and doping dependence of the Bi-Sr-Ca-Cu-O electronic structure and fluctuation effects. *Physical Review B* **56**, 14185–14189 (1997).

[11] Fedorov, A. V., Valla, T., Johnson, P. D., Li, Q., Gu, G. D. & Koshizuka, N. Temperature Dependent Photoemission Studies of Optimally Doped Bi2Sr2CaCu2O8. *Physical Review Letters* **82**, 2179–2182 (1999).

[12] Keimer, B., Kivelson, S. A., Norman, M. R., Uchida, S. & Zaanen, J. From quantum matter to high-temperature superconductivity in copper oxides. *Nature* **518**, 179–186 (2015). URL https://doi.org/10.1038/nature14165.

[13] Fradkin, E., Kivelson, S. A. & Tranquada, J. M. Colloquium: Theory of intertwined orders in high temperature superconductors. *Rev. Mod. Phys.* **87**, 457–482 (2015). URL https://link.aps.org/doi/10.1103/RevModPhys.87.457.

[14] Chubukov, A. & Hirschfeld, P. J. Iron-based superconductors, seven years later. *Physics today* **68**, 46–52 (2015).

[15] Takahashi, H., Igawa, K., Arii, K., Kamihara, Y., Hirano, M. & Hosono, H. Superconductivity at 43 K in an iron-based layered compound LaO1-xFxFeAs. *Nature* **453**, 376–378 (2008).

[16] Fernandes, R., Chubukov, A. & Schmalian, J. What drives nematic order in iron-based superconductors? *Nature Physics* **10**, 97–104 (2014). URL https://doi.org/10.1038/nphys2877.

[17] Huang, J., Yu, R., Xu, Z., Zhu, J.-X., Oh, J. S., Jiang, Q., Wang, M., Wu, H., Chen, T., Denlinger, J. D., Mo, S.-K., Hashimoto, M., Michiardi, M., Pedersen, T. M., Gorovikov, S., Zhdanovich, S., Damascelli, A., Gu, G., Dai, P., Chu, J.-H., Lu, D., Si, Q., Birgeneau, R. J. & Yi, M. Correlation-driven electronic reconstruction in $FeTe_{1-x}Se_x$. *Communications Physics* **5**, 29 (2022). URL https://doi.org/10.1038/s42005-022-00805-6.

[18] Basov, D. N. & Chubukov, A. V. Manifesto for a higher Tc. *Nature Physics* **7**, 272–276 (2011).

[19] Fernandes, R. M. & Chubukov, A. V. Low-energy microscopic models for iron-based superconductors: a review. *Reports on Progress in Physics* **80**, 014503 (2016).

[20] Hosoi, S., Matsuura, K., Ishida, K., Wang, H., Mizukami, Y., Watashige, T., Kasahara, S., Matsuda, Y. & Shibauchi, T. Nematic quantum critical point without magnetism in $FeSe_{1-x}S_x$ superconductors. *Proceedings of the National Academy of Sciences* **113**, 8139–8143 (2016). URL https://doi.org/10.1073/pnas.1605806113.

[21] Coldea, A. I. Electronic Nematic States Tuned by Isoelectronic Substitution in Bulk $FeSe_{1-x}S_x$. *Frontiers in Physics* **8**, 528 (2021). URL https://www.frontiersin.org/article/10.3389/fphy.2020.594500.

[22] Zhang, P., Yaji, K., Hashimoto, T., Ota, Y., Kondo, T., Okazaki, K., Wang, Z., Wen, J., Gu, G. D., Ding, H. & Shin, S. Observation of topological superconductivity on the surface of an iron-based superconductor. *Science* **360**, 182–186 (2018).

[23] Hanaguri, T., Iwaya, K., Kohsaka, Y., Machida, T., Watashige, T., Kasahara, S., Shibauchi, T. & Matsuda, Y. Two distinct superconducting pairing states divided by the nematic end point in $FeSe_{1-x}S_x$. *Science Advances* **4**, eaar6419 (2018). URL https://www.science.org/doi/abs/10.1126/sciadv.aar6419.

[24] Damascelli, A., Hussain, Z. & Shen, Z.-X. Angle-resolved photoemission studies of the cuprate superconductors. *Reviews of modern physics* **75**, 473 (2003).

[25] Yazdani, A., da Silva Neto, E. H. & Aynajian, P. Spectroscopic imaging of strongly correlated electronic states. *Annual Review of Condensed Matter Physics* **7**, 11–33 (2016).

[26] Comin, R. & Damascelli, A. Resonant X-Ray Scattering Studies of Charge Order in Cuprates. *Annual Review of Condensed Matter Physics* **7**, 369–405 (2016).

[27] Binnig, G., Rohrer, H., Gerber, C. & Weibel, E. Surface Studies by Scanning Tunneling Microscopy. *Physical Review Letters* **49**, 57–61 (1982).

[28] Tersoff, J. & Hamann, D. R. Theory of the scanning tunneling microscope. *Physical Review B* **31**, 805–813 (1985).

[29] Böhmer, A. E., Chu, J.-H., Lederer, S. & Yi, M. Nematicity and nematic fluctuations in iron-based superconductors. *Nature Physics* **18**, 1412–1419 (2022).

[30] Böhmer, A. E. & Kreisel, A. Nematicity, magnetism and superconductivity in FeSe. *Journal of Physics: Condensed Matter* **30**, 023001 (2017).

[31] Stewart, G. R. Unconventional superconductivity. *Advances in Physics* **66**, 75–196 (2017). URL https://doi.org/10.1080/00018732.2017.1331615.

[32] Shibauchi, T., Hanaguri, T. & Matsuda, Y. Exotic Superconducting States in FeSe-based Materials. *Journal of the Physical Society of Japan* **89**, 102002 (2020). URL https://doi.org/10.7566/JPSJ.89.102002.

[33] Coldea, A. I. & Watson, M. D. The key ingredients of the electronic structure of FeSe. *Annual Review of Condensed Matter Physics* **9**, 125–146 (2018).

[34] Coldea, A. I., Blake, S. F., Kasahara, S., Haghighirad, A. A., Watson, M. D., Knafo, W., Choi, E. S., McCollam, A., Reiss, P., Yamashita, T. *et al.* Evolution of the low-temperature Fermi surface of superconducting FeSe 1- x S x across a nematic phase transition. *npj Quantum Materials* **4**, 1–7 (2019).

[35] Yi, M., Lu, D., Chu, J.-H., Analytis, J. G., Sorini, A. P., Kemper, A. F., Moritz, B., Mo, S.-K., Moore, R. G., Hashimoto, M., Lee, W.-S., Hussain, Z., Devereaux, T. P., Fisher, I. R. & Shen, Z.-X. Symmetry-breaking orbital anisotropy observed for detwinned Ba(Fe 1- x Co x) 2 As 2 above the spin density wave transition. *Proceedings of the National Academy of Sciences* **108**, 6878–6883 (2011).

[36] Chu, J.-H., Analytis, J. G., Press, D., De Greve, K., Ladd, T. D., Yamamoto, Y. & Fisher, I. R. In-plane electronic anisotropy in underdoped Ba(Fe1-xCox)2As2 revealed by partial detwinning in a magnetic field. *Physical Review B* **81**, 214502 (2010).

[37] Nakajima, M., Ishida, S., Tomioka, Y., Kihou, K., Lee, C. H., Iyo, A., Ito, T., Kakeshita, T., Eisaki, H. & Uchida, S. Effect of Co Doping on the In-Plane Anisotropy in the Optical Spectrum of Underdoped Ba(Fe1-xCox)2As2. *Physical Review Letters* **109**, 217003 (2012).

[38] Kasahara, S., Shi, H. J., Hashimoto, K., Tonegawa, S., Mizukami, Y., Shibauchi, T., Sugimoto, K., Fukuda, T., Terashima, T., Nevidomskyy, A. H. & Matsuda, Y. Electronic nematicity above the structural and superconducting transition in BaFe2(As1-xPx)2. *Nature* **486**, 382–385 (2012).

[39] Margadonna, S., Takabayashi, Y., McDonald, M. T., Kasperkiewicz, K., Mizuguchi, Y., Takano, Y., Fitch, A. N., Suard, E. & Prassides, K. Crystal structure of the new FeSe1-x superconductor. *Chemical Communications* 5607 (2008).

[40] Hsu, F.-C., Luo, J.-Y., Yeh, K.-W., Chen, T.-K., Huang, T.-W., Wu, P. M., Lee, Y.-C., Huang, Y.-L., Chu, Y.-Y., Yan, D.-C. & Wu, M.-K. Superconductivity in the PbO-type structure α-FeSe. *Proceedings of the National Academy of Sciences* **105**, 14262–14264 (2008).

[41] Mizuguchi, Y., Tomioka, F., Tsuda, S., Yamaguchi, T. & Takano, Y. Superconductivity at 27K in tetragonal FeSe under high pressure. *Applied Physics Letters* **93**, 152505 (2008).

[42] Böhmer, A., Arai, T., Hardy, F., Hattori, T., Iye, T., Wolf, T., Löhneysen, H., Ishida, K. & Meingast, C. Origin of the Tetragonal-to-Orthorhombic Phase Transition in FeSe: A Combined Thermodynamic and NMR Study of Nematicity. *Physical Review Letters* **114**, 027001 (2015).

[43] Chu, J.-H., Kuo, H.-H., Analytis, J. G. & Fisher, I. R. Divergent nematic susceptibility in an iron arsenide superconductor. *Science* **337**, 710–712 (2012).

[44] Watson, M., Kim, T., Haghighirad, A., Davies, N., McCollam, A., Narayanan, A., Blake, S., Chen, Y., Ghannadzadeh, S., Schofield, A. *et al.* Emergence of the nematic electronic state in FeSe. *Physical Review B* **91**, 155106 (2015).

[45] Watson, M. D., Haghighirad, A. A., Rhodes, L. C., Hoesch, M. & Kim, T. K. Electronic anisotropies revealed by detwinned angle-resolved photo-emission spectroscopy measurements of FeSe. *New Journal of Physics* **19**, 103021 (2017).

[46] Rhodes, L. C., Böker, J., Müller, M. A., Eschrig, M. & Eremin, I. M. Non-local d_{xy} nematicity and the missing electron pocket in FeSe. *npj Quantum Materials* **6**, 45 (2021). URL https://doi.org/10.1038/s41535-021-00341-6.

[47] Yi, M., Pfau, H., Zhang, Y., He, Y., Wu, H., Chen, T., Ye, Z., Hashimoto, M., Yu, R., Si, Q., Lee, D.-H., Dai, P., Shen, Z.-X., Lu, D. & Birgeneau, R. Nematic Energy Scale and the Missing Electron Pocket in FeSe. *Physical Review X* **9**, 041049 (2019).

[48] Watson, M. D., Kim, T. K., Rhodes, L. C., Eschrig, M., Hoesch, M., Haghighirad, A. A. & Coldea, A. I. Evidence for unidirectional nematic bond ordering in FeSe. *Phys. Rev. B* **94**, 201107 (2016). URL https://link.aps.org/doi/10.1103/PhysRevB.94.201107.

[49] Watson, M., Kim, T., Haghighirad, A., Blake, S., Davies, N., Hoesch, M., Wolf, T. & Coldea, A. Suppression of orbital ordering by chemical pressure in FeSe 1- x S x. *Physical Review B* **92**, 121108 (2015).

[50] van Delft, D. & Kes, P. The discovery of superconductivity. *Physics Today* **63**, 38–43 (2010).

[51] Stewart, G. R. Heavy-fermion systems. *Reviews of Modern Physics* **56**, 755–787 (1984).

[52] Tsuei, C. C. & Kirtley, J. R. Pairing symmetry in cuprate superconductors. *Reviews of Modern Physics* **72**, 969–1016 (2000).

[53] Chubukov, A. Pairing Mechanism in Fe-Based Superconductors. *Annual Review of Condensed Matter Physics* **3**, 57–92 (2012).

[54] Wiecki, P., Rana, K., Böhmer, A. E., Lee, Y., Bud'ko, S. L., Canfield, P. C. & Furukawa, Y. Persistent correlation between superconductivity and antiferromagnetic fluctuations near a nematic quantum critical point in $FeSe_{1-x}S_x$. *Phys. Rev. B* **98**, 020507 (2018). URL https://link.aps.org/doi/10.1103/PhysRevB.98.020507.

[55] Sato, Y., Kasahara, S., Taniguchi, T., Xing, X., Kasahara, Y., Tokiwa, Y., Yamakawa, Y., Kontani, H., Shibauchi, T. & Matsuda, Y. Abrupt change of the superconducting gap structure at the nematic critical point in $FeSe_{1-x}S_x$. *Proceedings of the National Academy of Sciences* **115**, 1227–1231 (2018). URL https://www.pnas.org/content/115/6/1227.

[56] Sprau, P. O., Kostin, A., Kreisel, A., Böhmer, A. E., Taufour, V., Canfield, P. C., Mukherjee, S., Hirschfeld, P. J., Andersen, B. M. & Davis, J. C. S. Discovery of orbital-selective Cooper pairing in FeSe. *Science* **357**, 75–80 (2017). URL https://www.science.org/doi/abs/10.1126/science.aal1575.

[57] Grüner, G. The dynamics of charge-density waves. *Reviews of Modern Physics* **60**, 1129–1181 (1988).

[58] Johannes, M., Mazin, I. & Howells, C. Fermi-surface nesting and the origin of the charge-density wave in¡mml:math xmlns:mml="http://www.w3.org/1998/Math/MathML" display="inline"¿¡mml:mrow¿¡mml:mi mathvariant="normal"¿Nb¡/mml:mi¿¡mml:msub¿¡mml:mi mathvariant="normal"¿Se¡/mml:mi¿¡mml:mn¿2¡/mml:mn¿¡/mml:msub¿¡/mml:mrow¿¡/mml:math¿. *Physical Review B* **73**, 205102 (2006).

[59] Walker, M., Scott, K., Boyle, T. J., Byland, J. K., Bötzel, S., Zhao, Z., Day, R. P., Zhdanovich, S., Gorovikov, S., Pedersen, T. M., Klavins, P., Damascelli, A., Eremin, I. M., Gozar, A., Taufour, V. & da Silva Neto, E. H. Electronic stripe patterns near the fermi level of tetragonal Fe(Se,S). *npj Quantum Materials* **8** (2023).

[60] Böhmer, A. E., Taufour, V., Straszheim, W. E., Wolf, T. & Canfield, P. C. Variation of transition temperatures and residual resistivity ratio in vapor-grown FeSe. *Physical Review B* **94**, 024526 (2016).

[61] Cvetkovic, V. & Vafek, O. Space group symmetry, spin-orbit coupling, and the low-energy effective Hamiltonian for iron-based superconductors. *Phys. Rev. B* **88**, 134510 (2013). URL https://link.aps.org/doi/10.1103/PhysRevB.88.134510.

[62] Zhang, Y., Lee, J. J., Moore, R. G., Li, W., Yi, M., Hashimoto, M., Lu, D. H., Devereaux, T. P., Lee, D.-H. & Shen, Z.-X. Superconducting Gap Anisotropy in Monolayer FeSe Thin Film. *Phys. Rev. Lett.* **117**, 117001 (2016). URL https://link.aps.org/doi/10.1103/PhysRevLett.117.117001.

[63] Kushnirenko, Y. S., Fedorov, A. V., Haubold, E., Thirupathaiah, S., Wolf, T., Aswartham, S., Morozov, I., Kim, T. K., Büchner, B. & Borisenko, S. V. Three-dimensional superconducting gap in FeSe from angle-resolved photoemission spectroscopy. *Phys. Rev. B* **97**, 180501 (2018). URL https://link.aps.org/doi/10.1103/PhysRevB.97.180501.

[64] da Silva Neto, E. H., Aynajian, P., Frano, A., Comin, R., Schierle, E., Weschke, E., Gyenis, A., Wen, J., Schneeloch, J., Xu, Z., Ono, S., Gu, G., Le Tacon, M. & Yazdani, A. Ubiquitous Interplay Between Charge Ordering and High-Temperature Superconductivity in Cuprates. *Science* **343**, 393–396 (2014). URL http://www.sciencemag.org/content/343/6169/393.abstract.

[65] Yim, C. M., Trainer, C., Aluru, R., Chi, S., Hardy, W. N., Liang, R., Bonn, D. & Wahl, P. Discovery of a strain-stabilised smectic electronic order in LiFeAs. *Nature Communications* **9**, 1–7 (2018). URL https://doi.org/10.1038/s41467-018-04909-y.

[66] Li, W., Zhang, Y., Deng, P., Xu, Z., Mo, S.-K., Yi, M., Ding, H., Hashimoto, M., Moore, R., Lu, D.-H. *et al.* Stripes developed at the strong limit of nematicity in FeSe film. *Nature Physics* **13**, 957–961 (2017). URL https://doi.org/10.1038/nphys4186.

[67] Yuan, Y., Fan, X., Wang, X., He, K., Zhang, Y., Xue, Q.-K. & Li, W. Incommensurate smectic phase in close proximity to the high-T_c superconductor FeSe/$SrTiO_3$. *Nature Communications* **12**, 1–9 (2021). URL https://doi.org/10.1038/s41467-021-22516-2.

[68] Lahiri, A., Klein, A. & Fernandes, R. M. Defect-induced electronic smectic state at the surface of nematic materials. *Phys. Rev. B* **106**, L140503 (2022). URL https://link.aps.org/doi/10.1103/PhysRevB.106.L140503.

[69] Villar Arribi, P. & de' Medici, L. Hund-Enhanced Electronic Compressibility in FeSe and its Correlation with T_c. *Phys. Rev. Lett.* **121**, 197001 (2018). URL https://link.aps.org/doi/10.1103/PhysRevLett.121.197001.

[70] Reiss, P., Watson, M. D., Kim, T. K., Haghighirad, A. A., Woodruff, D. N., Bruma, M., Clarke, S. J. & Coldea, A. I. Suppression of electronic correlations by chemical pressure from FeSe to FeS. *Phys. Rev. B* **96**, 121103 (2017). URL https://link.aps.org/doi/10.1103/PhysRevB.96.121103.

[71] Boyle, T. J., Walker, M., Ruiz, A., Schierle, E., Zhao, Z., Boschini, F., Sutarto, R., Boyko, T. D., Moore, W., Tamura, N., He, F., Weschke, E., Gozar, A., Peng, W., Komarek, A. C., Damascelli, A., Schüßler-Langeheine, C., Frano, A., da Silva Neto, E. H. & Blanco-Canosa, S. Large response of charge stripes to uniaxial stress in LNSCO-125. *Physical Review Research* **3**, l022004 (2021).

[72] Fujita, M., Goka, H., Yamada, K. & Matsuda, M. Competition between Charge- and Spin-Density-Wave Order and Superconductivity in LBCO. *Physical Review Letters* **88**, 167008 (2002).

[73] Klauss, H.-H., Wagener, W., Hillberg, M., Kopmann, W., Walf, H., Litterst, F. J., Hücker, M. & Büchner, B. From Antiferromagnetic Order to Static Magnetic Stripes: The Phase Diagram of LESCO. *Physical Review Letters* **85**, 4590–4593 (2000).

[74] Hoffman, J., McElroy, K., Lee, D.-H., Lang, K., Eisaki, H., Uchida, S. & Davis, J. Imaging quasiparticle interference in Bi2Sr2CaCu2O8+ δ. *Science* **297**, 1148–1151 (2002).

[75] Ghiringhelli, G., Le Tacon, M., Minola, M., Blanco-Canosa, S., Mazzoli, C., Brookes, N. B., De Luca, G. M., Frano, A., Hawthorn, D. G., He, F., Loew, T., Sala, M. M., Peets, D. C., Salluzzo, M., Schierle, E., Sutarto, R., Sawatzky, G. A., Weschke, E., Keimer, B. & Braicovich, L. Long-Range Incommensurate Charge Fluctuations in (Y,Nd)Ba2Cu3O6+x. *Science* **337**, 821–825 (2012). URL https://science.sciencemag.org/content/337/6096/821.

[76] Miao, H., Fumagalli, R., Rossi, M., Lorenzana, J., Seibold, G., Yakhou-Harris, F., Kummer, K., Brookes, N., Gu, G., Braicovich, L., Ghiringhelli, G. & Dean, M. Formation of Incommensurate Charge Density Waves in Cuprates. *Physical Review X* **9**, 031042 (2019).

[77] Achkar, A. J., Zwiebler, M., McMahon, C., He, F., Sutarto, R., Djianto, I., Hao, Z., Gingras, M. J. P., Hücker, M., Gu, G. D., Revcolevschi, A., Zhang, H., Kim, Y.-J., Geck, J. & Hawthorn, D. G. Nematicity in stripe-ordered cuprates probed via resonant x-ray scattering. *Science* **351**, 576–578 (2016).

[78] Hücker, M., v. Zimmermann, M., Debessai, M., Schilling, J. S., Tranquada, J. M. & Gu, G. D. Spontaneous Symmetry Breaking by Charge Stripes in the High Pressure Phase of Superconducting $La_{1.875}Ba_{0.125}CuO_4$. *Phys. Rev. Lett.* **104**, 057004 (2010).

[79] Fink, J., Soltwisch, V., Geck, J., Schierle, E., Weschke, E. & Büchner, B. Phase diagram of charge order in $La_{1.8-x}Eu_{0.2}Sr_xCuO_4$ from resonant soft x-ray diffraction. *Physical Review B* **83**, 092503 (2011).

[80] Achkar, A., Zwiebler, M., McMahon, C., He, F., Sutarto, R., Djianto, I., Hao, Z., Gingras, M. J., Hücker, M., Gu, G. *et al.* Nematicity in stripe-ordered cuprates probed via resonant x-ray scattering. *Science* **351**, 576–578 (2016).

[81] Blanco-Canosa, S., Schierle, E., Li, Z. W., Guo, H., Adachi, T., Koike, Y., Sobolev, O., Weschke, E., Komarek, A. C. & Schüßler-Langeheine, C. Magnetic field effect in stripe-ordered 214 $(La_{1.6-x}Nd_{0.4})Sr_xCuO_4$ and $La_{2-x}Ba_xCuO_4$ superconducting cuprates studied by resonant soft x-ray scattering. *Phys. Rev. B* **97**, 195130 (2018). URL https://link.aps.org/doi/10.1103/PhysRevB.97.195130.

[82] Hicks, C. W., Barber, M. E., Edkins, S. D., Brodsky, D. O. & Mackenzie, A. P. Piezoelectric-based apparatus for strain tuning. *Review of Scientific Instruments* **85**, 065003 (2014). URL https://doi.org/10.1063/1.4881611. https://doi.org/10.1063/1.4881611.

[83] Kim, H.-H., Souliou, S. M., Barber, M. E., Lefrançois, E., Minola, M., Tortora, M., Heid, R., Nandi, N., Borzi, R. A., Garbarino, G., Bosak, A., Porras, J., Loew, T., König, M., Moll, P. J. W., Mackenzie, A. P., Keimer, B., Hicks, C. W. & Le Tacon, M. Uniaxial pressure control of competing orders in a high-temperature superconductor. *Science* **362**, 1040–1044 (2018). URL https://science.sciencemag.org/content/362/6418/1040. https://science.sciencemag.org/content/362/6418/1040.full.pdf.

[84] Kim, H.-H., Lefrançois, E., Kummer, K., Fumagalli, R., Brookes, N., Betto, D., Nakata, S., Tortora, M., Porras, J., Loew, T., Barber, M., Braicovich, L., Mackenzie, A., Hicks, C., Keimer, B., Minola, M. & Tacon, M. L. Charge Density Waves in YBCO Probed by Resonant X-Ray Scattering under Uniaxial Compression. *Physical Review Letters* **126**, 037002 (2021).

[85] Migliori, A., Sarrao, J., Visscher, W. M., Bell, T., Lei, M., Fisk, Z. & Leisure, R. Resonant ultrasound spectroscopic techniques for measurement of the elastic moduli of solids. *Physica B: Condensed Matter* **183**, 1 – 24 (1993). URL http://www.sciencedirect.com/science/article/pii/092145269390048B.

[86] Gugenberger, F., Meingast, C., Roth, G., Grube, K., Breit, V., Weber, T., Wühl, H., Uchida, S. & Nakamura, Y. Uniaxial pressure dependence of T_c from high-resolution dilatometry of untwinned $La_{2-x}Sr_xCuO_4$ single crystals. *Phys. Rev. B* **49**, 13137–13142 (1994). URL https://link.aps.org/doi/10.1103/PhysRevB.49.13137.

[87] Perea-Solano, B. Cryogenic Silicon Microstrip Detector Modules for LHC (2004). URL https://cds.cern.ch/record/802087. Presented on Jul 2004.

[88] Arpaia, R., Caprara, S., Fumagalli, R., Vecchi, G. D., Peng, Y. Y., Andersson, E., Betto, D., Luca, G. M. D., Brookes, N. B., Lombardi, F., Salluzzo, M., Braicovich, L., Castro, C. D., Grilli, M. & Ghiringhelli, G. Dynamical charge density fluctuations pervading the phase diagram of a Cu-based high-T_c superconductor. *Science* **365**, 906–910 (2019).

[89] Boschini, F., Minola, M., Sutarto, R., Schierle, E., Bluschke, M., Das, S., Yang, Y., Michiardi, M., Shao, Y. C., Feng, X., Ono, S., Zhong, R. D., Schneeloch, J. A., Gu, G. D., Weschke, E., He, F., Chuang, Y. D., Keimer, B., Damascelli, A., Frano, A. & da Silva Neto, E. H. Dynamic electron correlations with charge order wavelength along all directions in the copper oxide plane. *Nature Communications* **12**, 597 (2021). URL https://doi.org/10.1038/s41467-020-20824-7.

[90] Guguchia, Z., Das, D., Wang, C. N., Adachi, T., Kitajima, N., Elender, M., Brückner, F., Ghosh, S., Grinenko, V., Shiroka, T., Müller, M., Mudry, C., Baines, C., Bartkowiak, M., Koike, Y., Amato, A., Tranquada, J. M., Klauss, H.-H., Hicks, C. W. & Luetkens, H. Using Uniaxial Stress to Probe the Relationship between Competing Superconducting States in a Cuprate with Spin-stripe Order. *Phys. Rev. Lett.* **125**, 097005 (2020).

[91] Arumugam, S., Môri, N., Takeshita, N., Takashima, H., Noda, T., Eisaki, H. & Uchida, S. Competition of Static Stripe and Superconducting Phases in $La_{1.48}Nd_{0.4}Sr_{0.12}CuO_4$ Controlled by Pressure. *Phys. Rev. Lett.* **88**, 247001 (2002). URL https://link.aps.org/doi/10.1103/PhysRevLett.88.247001.